Low Resolution Spectral Templates For Galaxies From 0.2 – 10μm

R.J. Assef[1], C.S. Kochanek[1], M. Brodwin[2], M.J.I. Brown[3], N. Caldwell[4], R.J. Cool[5], P. Eisenhardt[2], D. Eisenstein[5], A.H. Gonzalez[6], B.T. Jannuzi[7] C. Jones[4], E. McKenzie[8], S.S. Murray[4], D. Stern[2]

ABSTRACT

We built an optimal basis of low resolution templates for galaxies over the wavelength range from 0.2 to 10 μm using a variant of the algorithm presented by Budavari et al. (2000). We derived them using eleven bands of photometry from the NDWFS, FLAMEX, zBoötes and IRAC Shallow surveys for 16033 galaxies in the NDWFS Boötes field with spectroscopic redshifts measured by the AGN and Galaxy Evolution Survey. We also developed algorithms to accurately determine photometric redshifts, K corrections and bolometric luminosities using these templates. Our photometric redshifts have an accuracy of $\sigma_z/(1+z) = 0.04$ when clipped to the best 95%. We used these templates to study the spectral type distribution in the field and to estimate luminosity functions of galaxies as a function of redshift and spectral type. In particular, we note that the 5-8μm color distribution of galaxies is bimodal, much like the optical g–r colors.

Subject headings: galaxies: photometry — galaxies: distances and redshifts — galaxies: luminosity function

[1]Department of Astronomy, The Ohio State University, 140 W. 18th Ave., Columbus, OH 43210

[2]Jet Propulsion, California Institute of Technology, Mail Stop 169-506, Pasadena, CA91109

[3]School of Physics, Monash University, Clayton 3800, Victoria, Australia

[4]Harvard/Smithsonian Center for Astrophysics, 60 Garden St., MS-67, Cambridge, MA 02138

[5]Steward Observatory, University of Arizona, 933 N Cherry Ave., Tucson, AZ 85121

[6]Department of Astronomy, University of Florida, Gainesville, FL 32611-2055

[7]KPNO/NOAO, 950 N. Cherry Ave., P.O. Box 26732, Tucson, AZ 85726

[8]Department of Physics and Astronomy, Colgate University, 13 Oak Drive, Hamilton, NY 13346

1. Introduction

Imaging surveys are a very important and common tool in astronomy. Large wide field surveys, such as the Two-Micron All Sky Survey (2MASS; Skrutskie et al. 2006) and the Sloan Digital Sky Survey (SDSS; York et al. 2000), and very deep ones, like GOODS (Dickinson et al. 2003) and the Hubble Ultra Deep Field (Beckwith et al. 2006), have radically improved our understanding of the universe. The large galaxy samples yielded by these surveys enable us, for example, to study the evolving space density of galaxies (Bell et al. 2004; Brown et al. 2007), baryon oscillations (Padmanabhan & Ray 2006) and the halo occupation distribution (Zehavi et al. 2005; Ouchi et al. 2005; Lee et al. 2006; White et al. 2007; Brown et al. in prep.). Astrophysical applications of these surveys require measurements of quantities such as the redshift, spectral type and rest frame and bolometric magnitudes of the galaxies. Due to the enormous number or faintness of the objects in these surveys, spectroscopic follow-up is extremely expensive, if not impossible, for the great majority of the sources. Even when spectra are available, they usually have low S/N, so most estimates of these quantities still have to come from broad-band photometry.

Extensive efforts over the last decade have shown that photometric redshifts estimates from broad-band photometry are reasonably accurate. Photometric redshift techniques can be divided into two main families: methods based on empirical relations between color and redshift that are usually implemented with neural networks (e.g. Wang et al. 1998; Brunner et al. 1999; Collister & Lahav 2004; Connolly et al. 1995), and methods based on Spectral Energy Distribution (SED) fitting techniques (e.g. Bolzonella et al. 2000; Benítez 2000). The first family of methods relies on the assumption that there is some relation between observed properties of galaxies and redshift that can be empirically calibrated using a training set of objects with both broad-band photometry and spectroscopic redshifts. These methods can automatically accommodate physical processes that are hard to model directly, such as dust extinction and emission, but they cannot be used for estimating K corrections, bolometric luminosities or redshifts outside the range of the training set. SED fitting techniques rely on model spectra to determine redshifts by minimizing the difference between observed and expected broad-band colors. This family of methods does not have redshift boundaries, as long as the observed rest-frame wavelengths overlap those of the template SEDs, and they can be used to determine K corrections and bolometric luminosities. They typically have larger uncertainties than the empirical methods (e.g., Csabai et al. 2003; Brodwin et al. 2006) and can fail badly for objects poorly described by the templates.

Templates used by the SED fitting methods are either derived from observations (e.g. Coleman, Wu & Weedman 1980; Kinney et al. 1996) or from stellar population synthesis models (e.g. Bruzual & Charlot 1993, 2003; Fioc & Rocca-Volmerange 1997). Most of these

templates have limited wavelength coverage. In particular, the popular Coleman, Wu & Weedman (1980) and Kinney et al. (1996) templates do not extend into the infrared and most synthetic templates have not been calibrated in this range or lack physical processes that operate at these wavelengths. Templates derived from observations sometimes come from very noisy spectra (e.g. Kinney et al. 1996), which could translate small systematic errors into large errors in the broad band colors. Templates from stellar population synthesis models do not suffer from this problem, but sometimes do a poor job reproducing observed properties of galaxies. For example, the red galaxy templates of Bruzual & Charlot (1993) agree with observed optical colors, but severely underestimate UV fluxes (e.g., see Figure 4 of Donas et al. 1995), and most models cannot reproduce the colors of star-forming galaxies because they do not include or cannot model nebular emission, dust and PAH emission features. While the `Pegase.2` models (Fioc & Rocca-Volmerange 1997) attempt to include these effects, their templates have not been calibrated particularly far into the infrared.

Budavari et al. (2000) and Csabai et al. (2000) developed a method that adjusts template SEDs in order to overcome these problems. The method uses a training data set to determine SEDs that accurately represent the galaxies and then uses the updated SEDs for photometric redshifts, K corrections and bolometric luminosities. A similar method has also been developed by Blanton et al. (2003a, also see Blanton et al. 2006), focusing mostly on K corrections, and by Feldmann et al. (2006), who implemented it, along with other features, in their ZEBRA package.

In this paper, we derive low resolution spectral templates for galaxies in the wavelength range 0.2–10 μm that accurately reproduce galaxy SEDs. We derive them using the extensive photometric observations of the NOAO Deep Wide-Field Survey (NDWFS; Jannuzi & Dey 1999) Boötes field combined with the redshifts from the spectroscopic observations of the AGN and Galaxy Evolution Survey (AGES; Kochanek et al. in prep) and a variant of the Budavari et al. (2000) method. AGES provides spectroscopic redshifts for approximately 17000 galaxies with $z \lesssim 1$, most of which have broad-band photometry from 0.4 to 8 μm.

In § 2 we describe the data we use to obtain the templates. In § 3 we describe the method used to derive the templates, as well as the algorithms used to determine bolometric luminosities, K corrections and photometric redshifts. In § 4 we derive the templates and apply the algorithms for K corrections and photometric redshifts to the galaxies from the AGES galaxy sample. And finally, in § 5, we study the spectral type distribution for approximately 65000 galaxies from the NDWFS Boötes field, based only on their photometry. We also use photometric redshifts and K corrections to determine luminosity functions for this field. Throughout the paper we assume the standard ΛCDM cosmology ($\Omega_{\rm M} = 0.3$, $\Omega_\Lambda = 0.7$, $\Omega_{\rm K} = 0$ and $H_0 = 70$ km/s/Mpc).

2. Data

The NOAO Deep Wide-Field Survey is a deep optical and near-infrared imaging survey that covers two 9.3 square degree fields, the Boötes and Cetus fields. Both fields were imaged in B_W (3500-4750 Å, peak at $\approx$ 4000 Å), R and I pass-bands to depths (5σ, $2''$ diameter apt.) of approximately 26.5, 26, and 25.5 AB magnitude. Both NDWFS fields have been completely imaged in the K and K_s bands to a limiting AB magnitude of 21.

In this paper we focus on the Boötes field observations, for which there has also been extensive coverage at other wavelengths. Specifically, we will also use the observations of the Flamingos Extragalactic Survey (FLAMEX; Elston et al. 2006), which covered about half of this field in the J and K_s bands, the z' band observations of the zBoötes survey (Cool 2006), and the IRAC Shallow Survey (Eisenhardt et al. 2004), which observed the field with the *Spitzer Space Telescope* Infrared Array Camera (IRAC; Fazio et al. 2004) in Channels 1, 2, 3 and 4 (3.6, 4.5, 5.8 and 8 μm respectively). We will refer to this last four bands as C1, C2, C3 and C4 respectively throughout the paper. It should be noted that there are also radio (FIRST, Becker et al. 1995;WENSS, Rengelink et al. 1997;WSRT, de Vries et al. 2002;NVSS, Condon et al. 1998), far-IR (MIPS, Weedman et al. 2006), X-ray (XBoötes, Murray et al. 2005) and UV (*GALEX*; Martin et al. 2005) observations of the NDWFS Boötes field that we do not currently use.

The AGN and Galaxy Evolution Survey is a redshift survey in the NDWFS Boötes field. It has obtained spectra for $\approx$ 20000 objects in the wavelength range from 3200Å to 9200Å with a resolution of $R \approx 1000$ using the 6.5m MMT telescope and the 300 fiber robotic Hectospec instrument (Fabricant et al. 2005). Spectroscopic redshifts have been measured for about 17000 galaxies in the field with $0 < z < 1$. The median redshift is approximately 0.31.

We derive the templates using a total of 16033 galaxies with spectroscopic redshifts and photometry in at least 6 of these 11 bands [B_W, R, I and K from NDWFS; z' from zBoötes; J and K_s from FLAMEX; and C1, C2, C3 and C4 from the IRAC Shallow Survey]. We required 6 bands so that we would always include some combination of optical and IR photometry for each galaxy, but requiring 5 or 7 would not affect our results. We use $6\farcs0$ aperture magnitudes to derive the templates and SExtractor (Bertin & Arnouts 1996) Kron-like magnitudes for estimates of the total flux. The photometry was corrected for Galactic extinction with the Schlegel et al. (1998) model. We cannot easily distinguish between non-detections and survey gaps from the existing photometry compilations, so we make no use of upper bounds.

The magnitudes measured by NDWFS and FLAMEX are in the Vega system. The

IRAC magnitudes are in their own system, which is based on the Kurucz model spectrum of Vega (see Reach et al. 2005). The z' magnitudes are in the AB system. Throughout the paper we keep these conventions – every magnitude computed is presented in its respective system. We will refer to the objects with both photometry and spectroscopic redshifts as the AGES galaxy sample.

3. Methods

In this section we present the algorithms developed to build the low resolution templates from the Boötes field observations and estimate K corrections, bolometric magnitudes and photometric redshifts. We have made the latter algorithms publicly available [1] as part of a Fortran-77 library that also incorporates other useful functions and can carry out the calculations for any set of filters specified by the user.

3.1. Templates

We build our templates using a variant of the approach proposed by Budavari et al. (2000). The flux $F_{i,b}$ of object i in band b is given by

$$F_{i,b} \;=\; c\ N_b \int_0^\infty \lambda^{-1} R_b(\lambda)\ f_i(\nu)\ d\lambda, \tag{1}$$

where N_b sets the normalization of the filter, $R_b(\lambda)$ is the filter bandpass response per photon of wavelength λ, c is the speed of light, and $f_i(\nu)$ is the object's observed spectrum measured in energy per unit area per unit time per unit frequency. In general, the spectra of a sample of galaxies will not be fully independent of each other, but, instead, can be regarded as different combinations of a small set, or basis, of rest frame spectral templates $T_k(\nu)$. Thus, we can model the observed flux of an object as

$$F_{i,b}^{mod} \;=\; c\ N_b \left(\frac{10\mathrm{pc}}{D_{l,i}}\right)^2 \sum_k a_{i,k} \int_0^\infty \lambda^{-1} R_b(\lambda)\ (1+z_i)\ T_k\left[(1+z_i)\nu\right]\ d\lambda, \tag{2}$$

where $a_{i,k}$ is the contribution of spectral component k to the observed spectra, z_i is the redshift of the galaxy and $D_{l,i}$ is its luminosity distance. We have assigned a bolometric luminosity of $10^{10} L_\odot$ and a distance of 10pc to the template spectra (see § 3.2). This

[1] www.astronomy.ohio-state.edu/∼rjassef/lrt

relation can be discretized as

$$F_{i,b}^{mod} = (1+z_i)\ c\ N_b \left(\frac{10\mathrm{pc}}{D_{l,i}}\right)^2 \sum_k a_{i,k} \sum_{\lambda_n} S_{i,b,\lambda_n}\ T_{k,\nu_n}, \tag{3}$$

where the T_{k,ν_n} are the discretized templates and

$$S_{i,b,\lambda_n} = \int_{\lambda_n}^{\lambda_{n+1}} \lambda^{-1} R_b[(1+z_i)\lambda]\ d\lambda \tag{4}$$

is the sensitivity curve of filter b shifted to the redshift of the observed object and integrated over wavelength bin λ_n.

The main idea of the method is to use the observed colors of galaxies to fit for the spectral base components T_{k,ν_n} . Budavari et al. (2000) used as their initial guesses orthogonal spectral components derived from a Principal Component Analysis (PCA) decomposition of the Coleman, Wu & Weedman (1980) galaxy templates (CWW from here on). Keeping the best fit templates orthogonal to each other during the iterative procedure, their final templates correspond to the principal components of the observed galaxy spectra. One problem with such a decomposition is that the model spectrum can be unphysical (negative) in some regions unless there are priors on the permitted values of the $a_{i,k}$.

Here we use an alternate approach that limits the construction of unphysical spectra. We start from the Elliptical, Sbc and Im CWW templates, extended to the mid infrared with the Bruzual and Charlot synthetic models (Bruzual & Charlot 2003). To reproduce the mid-IR dust/PAH features of star forming galaxies that these models lack, we spliced onto the Sbc and Im models a combination of the mid-IR part of the Devriendt, Guiderdoni & Sadat (1999) M82 and VCC 1003 templates, as shown in Figure 1. We do not apply this modification to the Elliptical template. Since all three templates represent very different star formation histories (i.e. they have very different stellar populations), they form a physical but not orthogonal basis set for galaxy spectra. We will try to find the best modifications of these spectra over the range 0.2 – 10 μm which will fit the AGES galaxies subject to the restrictions that the template spectra are non-negative ($T_{k,\nu_n} \geq 0$) and that the spectrum of a galaxy is a non-negative sum of these templates ($a_{i,k} \geq 0$). We will refer to the templates as E, Sbc and Im throughout the paper since the final optical spectra are sufficiently similar to the starting points to retain the names.

Since we are building the template spectra with significantly higher wavelength resolution than the broad band filters, we need to keep the spectra from developing unphysical oscillatory structures during the fit. We optimize the function

$$G = \chi^2 + \frac{1}{\eta^2} H, \tag{5}$$

where the χ^2 optimizes the fit to the templates, H forces the templates to be smooth, and η is a parameter that determines the strength of the smoothing. The goodness of fit to the data is

$$\chi^2 \;=\; \sum_{i,b} \left(\frac{F_{i,b} \;-\; F_{i,b}^{mod}}{\sigma_{i,b}} \right)^2 , \tag{6}$$

where $F_{i,b}$ is the observed flux of object i in band b with error $\sigma_{i,b}$, and the smoothing term

$$H \;=\; \sum_{k,n} \left(\log \frac{T_{k,\nu_n}}{Q_{k,\nu_n}} - \log \frac{T_{k,\nu_{n+1}}}{Q_{k,\nu_{n+1}}} \right)^2 \tag{7}$$

minimizes the logarithmic differences between the final templates (T_{k,ν_n}) and the initial templates (Q_{k,ν_n}). If a too small value of η is selected, the final templates will not be very different from their initial guesses and they will not be a good fit to the data. On the other hand, if a too large value of η is selected, the final templates will better fit the data but they will show non-physical oscillatory behavior. Selecting a value for η between these two extremes allows us to obtain galaxy templates that fit the photometry of the sample better than the initial ones but are still well behaved. Since the splices of the dust/PAH features are somewhat ad hoc, we decreased the weight of the logarithmic smoothing linearly with wavelength from 1 to 10 μm.

Offsets in the photometry can potentially bias the final best fit templates. Since our data covers a large range of redshifts, well sampled in every filter, we can compute corrections to the nominal photometric zero points of the AGES bands, as the overlapping regions between filters should break any degeneracies. These adjustments compensate both for the zero point errors and for any differences in the effective photometric aperture created by the differing PSFs of the observations. We can make these corrections to the extent that the smoothing functions and the underlying templates we are trying to find are not extremely different, since otherwise the smoothing can compensate for the differences by introducing some large scale behaviour into the zero point corrections rather than allowing the templates to change. We assume that the zero point corrections are small and not systematically related to each other, so all the large scale behaviour in them should come from this degeneracy. We remove any wavelength trend in the zero points by fitting a quadratic function to the zero point corrections and then rescaling the smoothing functions and the best fit templates.

We optimize equation (5) iteratively, starting with templates matching the initial templates, $T_{k,\nu_n} = Q_{k,\nu_n}$. We then iterate in steps: *(a)* estimate the galaxy weights $a_{i,k}$; *(b)* estimate zero point corrections by adjusting N_b; *(c)* sequentially optimize the templates and normalize them (see § 3.2); and *(d)* return to *(a)*. After every five iterations, we remove the large scale behaviour of the zero point corrections and rescale the smoothing functions and

templates. To optimize the templates we linearize the smoothing term assuming that the change in T_{k,ν_n} is small compared to Q_{k,ν_n}. As the resulting equations are linear, we can use a least squares algorithm in all the steps. Since we require that every coefficient for which we fit is positive (all $a_{i,k}$, $T_{k,\lambda}$ and N_b), we use the Non-Negative Least Squares Solver (NNLS) of Lawson & Hanson (1974). Our data sample contains objects with bad data points or with heavy AGN contamination, so we adjust the templates using only the 97% of the galaxies with the best fits.

3.2. Bolometric Luminosities and Template Normalization

We normalize the templates to have a constant "bolometric" luminosity of $10^{10}L_\odot$ over the wavelength range from $\lambda_{min} = 0.2\mu$m to $\lambda_{max} = 10\mu$m and to be at a distance of 10pc. The "bolometric" luminosity we use is defined as

$$L_{bol} = 4\pi D_l^2 \int_{\lambda_{min}}^{\lambda_{max}} f(\nu) \frac{d\lambda}{\lambda^2}, \tag{8}$$

where $f(\nu)$ is the observed SED of the object and D_l is its luminosity distance. Since the normalizations of the templates are the same, the total luminosity of a galaxy is simply

$$\frac{L_{bol}}{10^{10}L_\odot} = \sum_k a_k, \tag{9}$$

where the a_k are the galaxy weight coefficients of equation (2).

3.3. K Corrections

We can also use the templates to calculate K corrections (Oke & Sandage 1968; Hogg et al. 2002) for virtually any band as long as it is inside the wavelength range of the SED. This approach is similar to the one taken by Blanton et al. (2003a, also see Blanton et al. 2006).

When observing a galaxy through a certain bandpass, the portion of the rest frame SED of the object sampled by the bandpass will depend on the redshift of the object. The K correction can be defined as the correction needed to transform the observed magnitude through bandpass b of an object at redshift z to the magnitude we would measure for an object with the same SED and the same apparent bolometric magnitude but located at redshift z_0. We can write it as

$$m_b(z) = m_b(z_0) + K_b, \tag{10}$$

with the K correction K_b defined as

$$K_b \ = \ -2.5 \log \left[\frac{(1+z)}{(1+z_0)} \ \frac{\int_0^\infty \frac{R_b(\lambda)}{\lambda} f[(1+z)\nu] d\lambda}{\int_0^\infty \frac{R_b(\lambda)}{\lambda} f[(1+z_0)\nu] d\lambda} \right], \tag{11}$$

where $f(\nu)$ is the rest frame SED of the object in units of energy per unit area per unit time per unit wavelength. Usually, $z_0 = 0$, so that the magnitude is corrected to the rest frame. One alternative, adopted by the SDSS survey, is to set $z_0 = 0.1$, corresponding to the mode of their redshift distribution, as this minimizes the level of the corrections. Tables 3 and 4 show the absolute magnitudes of the templates as a function of redshift for the three and four templates model respectively we discuss in § 4. They can be used to determine K corrections for each of the AGES bands as well as other commonly used ones (see captions for more information).

3.4. Photometric Redshifts

Once we have derived the templates, it is very easy to estimate photometric redshifts for galaxies with fluxes f_b. For a given redshift, we find the best combination of the basis templates by minimizing

$$\chi^2(z, a_k) \ = \ \sum_b \left(\frac{f_b \ - \ c \ N_b \ (10\mathrm{pc}/D_l)^2 \ \sum_k a_k (1+z) \sum_\lambda S_{b,\lambda}(z) T_{k,\nu}}{\sigma_b} \right)^2, \tag{12}$$

where $S_{b,\lambda}(z)$ is equal to $S_{i,b,\lambda}$ from equation (4), to solve for $a_k(z)$. We continue to require that $a_k(z) \geq 0$ and find the solution with the NNLS algorithm. Then, with a grid search on the redshift values, we can obtain the optimal redshift for the galaxy.

We included a luminosity prior in our model to avoid selecting improbable luminosities as the best fits. Moreover, at very low redshifts, luminosity is a better distance measure than color. We set the probability for redshift z to be

$$P(z) \ \propto \ e^{-\chi^2(z)/2} \ \Phi[M] \ dV_{com}(z), \tag{13}$$

where $\Phi[M]$ is the luminosity function, the probability per unit of co-moving volume for a galaxy to have absolute magnitude M, and dV_{com} is the co-moving volume per unit redshift as a function of redshift. We assume the R-band luminosity function from the Las Campanas Redshift Survey (Lin et al. 1996), which is parametrized by a Schechter function (Schechter 1976) with $\alpha = -0.7$ and $M_\star = -21.4$. Our estimates might be improved by the use of spectral type priors (Benítez 2000; Feldmann et al. 2006), but they are not included in our present implementation. The K corrections in Tables 3 and 4 can also be used to estimate photometric redshifts (see caption for more information).

4. Results

4.1. Templates

Following the procedure outlined in § 3.1, we fit a model based on the three modified CWW templates described in § 3.1 to the AGES galaxy sample, using the photometry for the eleven bands described in § 2. The top panel of Figure 2 shows the number of objects used to derive the templates as a function of wavelength and the response curves of our eleven filters. The peaks in Figure 2 correspond to the mean wavelengths of the filters displaced by the redshift mode of our sample (~ 0.2). Given our standard template resolution, 160 logarithmically spaced wavelengths from 0.2–10 μm, these models have $N_{\rm DOF} = 90669$ degrees of freedom. We fit the data assuming the magnitude uncertainties are the larger of the measured errors and 0.05 mag. This minimum error was imposed so that low redshift galaxies with very small formal uncertainties did not dominate the fits.

To choose an appropriate smoothing weight η, we first fit the templates for a range of values. Figure 3 shows the best fitting templates for different weights η, the χ^2 of each fit and the residuals when compared to their initial guesses. In an ideal world, we would simply use the value of η that gives $\chi^2/N_{\rm DOF} = 1$. Unfortunately, we have imperfect errors for the data (e.g. bad data points and systematic errors from seeing variations) and imperfect templates that cannot encompass all physical parameters of real galaxies, so we are forced to adjust η on an empirical basis. Fortunately, the results are not very sensitive to our choice provided it is reasonable. With little smoothing ($\eta = 0.1$) we obtain a relatively low χ^2 but find very unnatural, rapidly oscillating spectra. On the other hand, very heavy smoothing ($\eta = 10^{-4}$) gives spectra that are not significantly different from their initial guesses and have significantly higher χ^2. Figure 4 shows the goodness of fit as a function of the smoothing weight, where we use a renormalized fit statistic defined such that $\hat{\chi}^2 \rightarrow N_{\rm DOF}$ in the limit of no smoothing ($\eta \rightarrow \infty$). Clearly, we want a value of η near the zone of the steep decrease in χ^2. More specifically, we want a value of η between approximately 10^{-2} and 10^{-3} to ensure that the templates have changed enough to fit the data well, but we have introduced no unphysical oscillations. Since the photometric redshifts, the K corrections and the bolometric luminosities are not very sensitive to this parameter as long as it is on this range, we choose $\eta = 0.004$ for our standard models. The resulting templates are shown in Figure 5 and are provided in Table 1. They produce a χ^2 of 201414, which for the 90669 degrees of freedom available gives $\chi^2/N_{\rm DOF} = 2.22$. The output templates are substantially different from our initial modified CWW ones and wildly different from the Bruzual & Charlot (2003) extended CWW templates. The fitted Elliptical template has a lower ratio of optical and mid-infrared to near-infrared emission, and the Sbc and Im templates have stronger PAH emissions in the mid-infrared.

Even though the three template model fits the data well, there is no physical reason why three templates should be enough to reconstruct the spectra for all galaxies in the sample. In particular, the initial templates are either actually star forming (Sbc, Im) or have had no recent star formation (Elliptical) – there is no intermediate age template. We tested a model with a 4$^{\mathrm{th}}$ template whose prior was a CWW Elliptical template combined with an A0 stellar spectra from the `Pegase.2` libraries (Fioc & Rocca-Volmerange 1997) to mimic an E+A/K+A spectrum. Since the dependence of the χ^2 deviations should not be extremely dependent on the types of templates that we are trying to fit, we will use $\eta = 0.004$ as above. The resulting templates are provided in Table 2 and produce a χ^2 of 146410, which for the 75028 degrees of freedom available gives $\chi^2/N_{\mathrm{DOF}} = 1.95$.

Figure 5 shows the best fit three and four template models compared to their initial guesses. They are clearly very different from their initial guesses. While the best fit elliptical and Sbc templates do not differ significantly from the previous case, the Im is very different. Even though Figure 4 shows that adding an additional template significantly reduces the χ^2 values, the formal improvement from adding the 4th template is only about 19σ based on the F-test. Moreover, as we shall see in § 4.3, adding the extra component also creates problems.

Compared to common template SEDs used in the literature, these templates do a significantly better job of tracing the observed color–color distribution of galaxies. Figures 6 and 7 show the color distributions of the AGES galaxies compared to the color ranges permitted by our basis of templates in the optical and mid-IR bands respectively for four redshift ranges. For comparison, we also show the optical color ranges spanned by six commonly used templates: the CWW Elliptical, Sbc, Scd and Im, and the Kinney et al. (1996) SB1 and SB2. The older templates represent the colors of galaxies poorly, especially in the redshift range 0.2–0.4, where the Sbc spiral template differs significantly from the observations. Notice that they span lines instead of full areas because they are single color points smeared by the redshift range. This can be somewhat overcome by interpolating between the templates, but this is highly dependent on the implementation of the interpolation scheme. In the mid-IR, we show for comparison the colors spanned by the Bruzual & Charlot (2003) extended CWW templates. These clearly do a very poor job reproducing the observed color–color distribution. In this same figure, note that the mid-IR distribution of galaxies at low redshift is strongly bimodal, resembling the g–r color distribution (e.g. Strateva et al. 2001; Blanton et al. 2003b; Madgwick et al. 2003; Bell et al. 2004).

Finally, it should be noted that while fitting the templates we also fitted for corrections to the nominal zero points of each of the AGES bands, relative to the B_W band. The zero points used are 3627.5, 3009.9, 2408.8, 3631.0, 1594.0, 666.7, 651.2, 277.5, 179.5, 116.6 and

63.1 Jy for the B_W, R, I, z', J, K_s, K, C1, C2, C3 and C4 bands respectively. The correction factors (relative to B_W) are 1.00, 1.01, 1.02, 1.03, 0.97, 1.00, 1.00, 1.06, 0.98, 1.01 and 1.03 respectively (the large discrepancy for the IRAC bands was also noted by Brodwin et al. (2006) and it seems to be related to aperture corrections for the IRAC PSF). In general, these should be viewed as corrections to a common mean photometric aperture rather than errors in the zero-point calibrations. Note that we cannot determine the absolute corrections since we are also fitting for the fluxes of the galaxies. These corrections could be improved by considering seeing variations between the individual observations, but we will not pursue this question at present.

4.2. K Corrections

As mentioned earlier, Blanton et al. (2003a) followed an approach similar to ours to determine K corrections. To test our code, we compare our K corrections for the AGES galaxy sample with those from the `kcorrect v4_1_4` code of Blanton et al. (2003a). Note that for this comparison we use the 4 template basis model, as it provides a better fit to the SEDs if the redshift is known (see § 4.1 and § 4.3).

Figure 8 shows the comparison for the B_W, R, I, J, z and K bands at low ($z < 0.3$) and high ($z > 0.3$) redshift. We do not examine the IRAC channels nor use them to fit the SEDs since `kcorrect v4_1_4` cannot model mid-IR fluxes. In general, the agreement is good, with a typical difference of less than about 0.1 magnitudes. The band with the largest dispersion is B_W. All bands show some deviation in the mean of a few hundredths of a magnitude, suggesting that there are some differences between the templates used by the codes. Notice that there is a smaller deviation at lower than at higher redshifts, which is expected since K corrections tend to be bigger at higher redshifts and `kcorrect` was largely calibrated at lower redshifts than the AGES sample.

4.3. Photometric Redshifts

Using the methods described in § 3.4, we obtain photometric redshifts for the AGES galaxy sample using the best fit Elliptical, Sbc and Im templates described in § 4.1, without considering the E+A component. We have so many sources that there is no particular reason to have a separate training set. The top left panel of Figure 9 shows a density contour plot of the photometric redshifts, z_p, compared to the spectroscopic ones, z_s, for the AGES galaxy sample. We show the dispersion in z_s at fixed z_p since this is the distribution relevant for

characterizing the errors in photometric redshifts. The central contours are tightly centered on the $z_p = z_s$ line, so the algorithm works well for the typical galaxy. The results for this are summarized in Table 5, as the "3 templates/complete sample", where we give the standard dispersion

$$\left[\frac{\sigma_z}{(1+z)}\right]^2 \equiv \frac{1}{N} \sum_{i=1}^{N} \left(\frac{z_p^i - z_s^i}{1+z_s^i}\right)^2, \tag{14}$$

the median offset of $z_p - z_s$, the ranges of $|z_p - z_s|/(1+z_s)$ encompassing 68.3, 95.5 and 99.7% of the distribution, and the dispersion Δz defined by equation (14) after clipping the sample to the 95% of the galaxies with the best $|z_p - z_s|$ to eliminate outliers. The distribution of errors has very non-Gaussian tails. For example, the region encompassing 68.3% of the galaxies is 1.5 times smaller than the dispersion. We explored the dependence of the redshift errors on redshift, luminosity and color, finding that the dominant effect is lower accuracy for bluer and fainter galaxies. For example, if we sort the galaxies by their fitted SED elliptical component fraction, $\hat{e}$, defined as

$$\hat{e} \equiv \frac{a_e}{a_e + a_s + a_i}, \tag{15}$$

where a_e, a_s and a_i are the Elliptical, Sbc and Im template components of the galaxy SED, we find that $\sigma_z/(1+z) = 0.047$ for the galaxies with $\hat{e} > 2/3$ and $\sigma_z/(1+z) = 0.071$ for $\hat{e} < 1/3$.

Recently, Brodwin et al. (2006) estimated redshifts for galaxies and AGNs in the IRAC Shallow survey using a hybrid algorithm between SED fitting and empirical neural networks, calibrated with AGES spectroscopic redshifts and photometry similar to that used in here. Due to the lack of dust/PAH features in their templates, SED fitting was only used for galaxies with $C3 - C4 < 1$, which corresponds to galaxies with little or no star formation, while neural networks were used for the rest of the galaxies and for the AGNs. Eliminating the need to use different methods for star-forming and quiescent galaxies was one of the motivations for our work. With this hybrid approach, Brodwin et al. (2006) obtained $\sigma_z/(1+z) = 0.105$ and $\Delta z = 0.047$ for galaxies, about a factor of 1.8 and 1.2 larger than what we obtained, although the two galaxy samples are not identical since Brodwin et al. (2006) used subset of AGES galaxies with measured C2 magnitudes rather than the full sample.

We repeated the calculations using the 4 template model as shown in the top right panel of Figure 9. The distribution statistics are again summarized in Table 5. The dispersion when using four templates is equal to that for three templates, while Δz is larger. This seems to show that even though the data are better fit using four templates rather than three, the freedom introduced by including an extra template broadens the photo-z distribution. Presumably this occurs because the four template model allows colors that expand beyond the observed range for galaxies (see Figs. 6 and 7) while the three template models do not.

We built the templates excluding the 3% of galaxies most poorly fit by them (see Figure 4). These poor fits are mostly caused by extreme star formation, AGN contamination and bad data. Figure 10 shows some examples of the worst and best fit galaxies. The flat continuum in the mid-infrared is the signature of an AGN (Stern et al. 2005). Figure 11 shows that galaxies that are poorly fit by the templates tend to have less reliable photometric redshifts, so we examined the accuracy for galaxies whose best fit photometric redshift yields a χ^2 smaller than the 90th percentile of its expected value. This criteria eliminates 25% of the original sample. As summarized in Table 5 and illustrated in the bottom panels of Figure 9, these χ^2-limited samples have distribution widths that are a factor of 1.2–1.4 smaller than for the sample as a whole, and by similar amounts for the 68.3, 95.5 and 99.7% intervals. We tried improving the photometric redshifts for objects with bad data by sequentially dropping individual magnitude measurements during the template fitting. While this greatly improved the fits, the redshift accuracy $\sigma_z/(1+z)$ worsened by 5–10% when considering the full sample. For objects that have AGN contamination, photometric redshifts could be improved by adding an AGN template when the galaxy templates fit poorly.

In these calculations we forced all a_k coefficients to be positive both while building the templates and while estimating the photometric redshifts. It is possible that this limitation might worsen the photometric redshifts, essentially by limiting the permitted range of star formation rates. When we tested this by recalculating the photometric redshifts without forcing $a_k \geq 0$, we found that the dispersion in the redshifts increases by factors of 1.3 and 1.5 for the 3 and 4 template models respectively. The problem is that the added freedom allows the accessible color space to expand well beyond that occupied by galaxies, thereby allowing good fits at bad redshifts. We also investigated the effects of the luminosity priors on the the photometric redshifts, and found out that while they improve the accuracy, the gain is marginal (5–10% effect in all cases).

To further test our photometric redshift determinations, we obtained the five bands of SDSS photometry for the galaxies in the AGES sample and estimated their redshifts based solely on this information. We find a dispersion of $\sigma_z/(1+z) = 0.086$ and $\Delta z = 0.052$, again with highly non-Gaussian tails. While these values are worse than what we had previously obtained for the same sample, as they are based on a smaller number of photometric bands, they prove the validity of our templates and algorithms. Csabai et al. (2003) estimated photometric redshifts for galaxies brighter than $r' = 18$ in the early data release of SDSS with a method similar to ours and found a standard deviation of $\sigma_{rms} = 0.045$. If we limit our SDSS sample to that magnitude, we find a very similar result of $\sigma_{rms} = 0.048$.

5. Spectral Classifications

We can now use the SED models for other applications, such as studying the spectral distribution of the galaxies in the sample. For this section, we use the full photometric galaxy sample of the Boötes field up to $I \leq 21$ mag, as derived from NDWFS, FLAMEX, zBoötes and IRAC observations. This "photometric" galaxy sample consists on approximately 80000 galaxies in total of which 69000 are usable because they have photometry in at least four of the eleven bands described in § 2 and have not been flagged by AGES for either having an AGN contribution or being near a bright star. We estimate photometric redshifts using the algorithm of § 3.4.

Figure 12 shows the distribution of galaxies as a function of their relative elliptical component $\hat{e}$ (see eqn. [15]). For this figure, and the rest of this section, we use the three template model for the reasons discussed in § 4.3. There are two components – one peak consists of nearly pure Elliptical galaxies, while the other covers a broad range of star forming galaxies. The spike at $\hat{e} = 0$ is a consequence of requiring $a_k \geq 0$ and contains $\sim 20\%$ of the objects. If we allow negative spectral coefficients, the distribution develops a smooth tail (see Fig. 12) where the best fitting SEDs subtract an Elliptical component from the Sbc/Im templates to reduce the 1.6μm emission peak. We inspected spectra of galaxies in the spike, and found that it is dominated by galaxies with obvious evidence of star formation, plus a number of galaxies with photometry issues ($\sim 10\%$). If we modify the templates by subtracting 20% of the Elliptical template from the two star forming ones, the spike shrinks, but at the cost of making the Sbc template unphysical and worsening the photometric redshifts. If we modify the components in this way and then refit the templates to the AGES sample using the method of § 3.1, they move back toward the original solution. A possible reason for this is the lack of a second parameter such as metallicity to differentiate between star forming galaxies, as the templates will converge to the typical galaxies. Lack of data also contributes to the formation of the spike. If we restrict the sample to galaxies with six or more bands of photometry, the fraction of galaxies in the spike goes down by about 20%. Photometric redshift errors also contribute, since the spike drops by 20% if we use spectroscopic redshifts and by 50% if we apply the χ^2 cuts of § 4.3 (see Fig. 12).

Figure 13 shows the distribution of the Elliptical template fraction $\hat{e}$ of the SEDs as a function of their bolometric luminosity L for three different redshift ranges. Note that while we use the $6\farcs0$ aperture fluxes to fit the templates, we correct to the total flux for the bolometric luminosity. We do this by scaling the best-fit SED by the ratio of the Kron-like SExtractor I band magnitude to the $6\farcs0$ one. In practice however, the I-band Kron-like photometry is sometimes affected by nearby bright stars beyond the AGES flagging, producing excessively bright magnitudes. To deal with this, we follow the approach of

Eisenstein et al. (in prep.) and use a total I-band magnitude produced from a weighted mean between the Kron-like measurement and the predicted one from the R-band measurement and the 6.″0 colors that favors the faintest of the two. To account for the volume and depth limitations of the survey, we use the $V/V_{\rm max}$ method (Schmidt 1968), to properly weight each bin for the effects of the magnitude limits. The density of each bin is given by

$$n \; = \; \sum_i \frac{1}{\min[\mathrm{V^i_{max}}, \mathrm{V_{max}}] - \mathrm{V_{min}}}, \tag{16}$$

where $V^i_{\rm max}$ is the co-moving volume to which galaxy i can be detected and $V_{\rm max}$ and $V_{\rm min}$ are the volumes corresponding to the upper and lower edges of the redshift bin. The $V^i_{\rm max}$ are easily calculated with our algorithm, since it only depends on the SED of the galaxy and the magnitude limits of the survey. In this figure we do not show the galaxies in the $\hat{e} = 0$ spike. As expected, we see a well-defined clump of galaxies with low star formation rate in all three redshift ranges, and also a less well-defined locus of star forming galaxies that spans a broader luminosity range. The latter group becomes less well-defined at higher redshifts. Notice that in the lowest redshift bin we cannot map the high star formation peak well mostly because of the problems discussed above with the blue spike of Figure 12.

Using the $V/V_{\rm max}$ method we also estimated B-band luminosity functions for the NDWFS Boötes field. We limited the survey to a central area of approximately 5.3 deg^2 that is uniformly sampled in all bands and contains ~ 43000 galaxies to $I < 21$. This is a conservative limit of the usable survey area, but it will not affect our results. As we did before, we excluded galaxies with a possible AGN contamination (1200 objects), photometry in fewer than 4 bands (1350) and near bright stars (2400), leaving us with a sample of approximately 39000 galaxies. Using our templates and algorithms, we predict the B-band (Bessell 1990) absolute magnitude of each galaxy. We corrected for the dropped objects as a simple sampling fraction correction. Naively implemented, the low luminosity tail of the LF estimates are dominated by $L \sim L_*$ objects with "catastrophic" photo-z errors. As discussed in section 4.3, a χ^2 cut can be implemented to minimize such systematic failures. After some iterations, we decided on eliminating the worst 10% of the objects,leaving the sample with ~ 35000 galaxies. This cut provides a good balance between minimizing the statistical uncertainties from the diminished number of objects and the systematic uncertainties from the photometric redshifts. Our estimated luminosity functions, scaled to the total number of galaxies in the selected sub-field (that is the ones used for the estimation plus the ones with bad fits and the ones near bright stars), are shown in Figure 14 for four redshift ranges and for four spectral type subdivisions: $0 \leq \hat{e} < 0.4$ (high star formation rate), $0.4 < \hat{e} < 0.8$ (intermediate star formation rate), $0.8 < \hat{e} \leq 1.0$ (low star formation rate) and $0.0 \leq \hat{e} \leq 1.0$ (all star formation rates). We estimated the errors by bootstrap re-sampling. This figure also shows the best fit Schechter functions (Schechter 1976) for each case, with the parameters

summarized in Table 6. We fit the Schechter functions only over the magnitude ranges where the functional form is appropriate, dropping the bins affected by the catalog magnitude limit and regions where there is an apparent upturn at faint magnitudes. This upturn is probably produced by a small artifact amplified by the $1/V_{max}$ weights. These present results are also limited by the photometry, with problems in the total (Kron) magnitudes for objects with bright neighbors affecting mostly the bright ends.

Brown et al. (2007) estimated the B-band luminosity functions of red galaxies in the NDWFS field. The left panels of Figure 15 shows their results compared to our $0.8 < \hat{e} \leq 1.0$ sample. Due to the different ways in which the samples were selected, we only expect them to agree on the bright end but not on the faint end slope or in the overall amplitude ϕ_*. Brown et al. (2007) defined their sample using the evolving and luminosity dependent rest frame U–V color criterion (eqn. [3] of Brown et al. 2007)

$$\mathrm{U - V > 1.40 - 0.25 - 0.08(M_V - 5\log h + 20.0) - 0.42(z - 0.05) + 0.07(z - 0.05)^2}, \quad (17)$$

which corresponds to the expected location of the red sequence in the $M_{\rm V}$ U–V plane displaced to the blue by 0.25 mag. Our criteria, on the other hand, corresponds to a non-evolving and luminosity independent U–V color (U–V $\gtrsim$ 1.1), so, by definition, our sample will include fewer faint galaxies than Brown et al. (2007). Moreover, the evolution of the criteria set by Brown et al. (2007) follows the evolution of the red sequence, becoming bluer with increasing redshift, so we expect the differences between the two luminosity functions to occur at brighter magnitudes at higher redshifts, as seen in Figure 15.

Wolf et al. (2003) carried out a similar analysis to ours, using galaxies from COMBO-17 with photometric redshifts and classifying them by their overall spectral shape rather than their colors. In particular, their *type 1* sample, defined as all galaxies with spectral types from Ellipticals to Sab spirals, is similar to our low star formation rate sample. We recalculated the luminosity functions using the COMBO-17 survey B-band for our early type sample, again keeping α fixed to the value from the $0.2 < z < 0.4$ redshifts bin, and found in general a good agreement with Wolf et al. (2003). The right panels of Figure 15 show our luminosity functions compared to those of Wolf et al. (2003) in the three redshift ranges where we overlap. The agreement is very good for the two lowest redshift ranges in the Figure, but somewhat worse for the highest one, although still compatible. A comparison with the rest of their results is not straightforward, as there is no trivial match between their selection criteria and ours for groups other than their *type 1*.

6. Conclusions

We have built an optimized basis of low resolution spectral templates for the wavelength range from 0.2–10 μm that accurately reproduce most galaxy SEDs. We used a variant of the Budavari et al. (2000) method to fit the SEDs of 17000 AGES galaxies with photometry in at least 6 of 11 possible bands. We considered a three template basis starting from the CWW Elliptical, Sbc and Im templates and a four template basis where we added an E+A post-starburst component. One novel feature of our approach is that we model each galaxy as a non-negative sum of templates, which markedly improves the match of the model to the observed color range of galaxies (see Figs. 6 and 7) and significantly improves photometric redshift estimates.

We applied these optimized templates to calculate accurate photometric redshifts. We find that while the four template models fit the galaxy SEDs better than the three template models when the redshift is known, they broaden the photometric redshifts errors by approximately 50%. Using the three templates basis, we showed that the accuracy of our method is $\sigma_z/(1+z) = 0.060$ ($\Delta z = 0.038$), with the accuracy being highest for early type galaxies. Many of the galaxies with poor photometric redshifts estimates are also poorly fit by the templates because of either bad photometric data points or AGN contamination. If we consider only galaxies having χ^2 values smaller than the 90th percentile of their expected value, the accuracy improves to $\sigma_z/(1+z) = 0.044$ ($\Delta z = 0.030$) when dropping the worst 5% of the redshifts. This is somewhat better than that obtained by Brodwin et al. (2006) for a very similar data set but using a hybrid approach that mixed SED fitting and neural networks. Our results are somewhat worse than those obtained by the ZEBRA code (Feldmann et al. 2006) for a COSMOS (Scoville et al. 2006) galaxy sample, but this is probably due to the very small number of degrees of freedom in their data set after fitting six redshift-dependent templates to a sample of only 866 galaxies that is then used to test those templates.

Besides photometric redshifts, we also applied these optimized templates to calculate accurate K corrections and bolometric luminosities. We compared the K corrections to those obtained using the `kcorrect v4_1_4` code of Blanton et al. (2003a) for the AGES galaxy sample and found a very good agreement between them. We have implemented our algorithms for calculating bolometric luminosities, K corrections and photometric redshifts, including our optimized template basis, in a public code[2] that can carry out the calculations for any set of filters provided by the user.

We applied these algorithms to the photometric galaxy sample of the NDWFS Boötes

[2]Code available at www.astronomy.ohio-state.edu/∼rjassef/lrt

field with $I \leq 21$ mag ($\sim$ 69000 galaxies) and studied the galaxy luminosity distribution as a function of redshift and star formation (parametrized by the early-type template fraction $\hat{e}$). We find that our algorithms reproduce the bimodal distribution of red and blue galaxies that has been observed as a function of color and magnitude in the SDSS (Strateva et al. 2001; Blanton et al. 2003b; Kauffmann et al. 2003), DEEP2 (Madgwick et al. 2003; Weiner et al. 2005) and COMBO-17 (Bell et al. 2004) surveys, for example. We have also shown that the mid-infrared color-color distribution of galaxies is strongly bimodal, resembling its optical counterpart, except that rather than a red clump and a blue cloud, it has a blue clump and a red cloud (Fig. 7). Finally, we used these algorithms to estimate the B-band luminosity functions of the field from a central region of the survey containing about 43000 galaxies. Our approach allows us to easily study them as a function of redshift and star formation. Our results, summarized in Figure 14 and Table 6, agree broadly with the results of Brown et al. (2007) and Wolf et al. (2003).

We wish thank Richard W. Pogge for lending us his expertize in analyzing spectra, Steve Willner for his suggestions and comments, and all the people in the NDWFS, FLAMEX and IRAC Shallow Survey collaborations that did not directly participate in this work. The AGES observations were obtained at the MMT Observatory, a joint facility of the Smithsonian Institution and the University of Arizona. This work made use of data products provided by the NOAO Deep Wide-Field Survey (Jannuzi & Dey 1999; Jannuzi et al. 2005; Dey et al. 2005), which is supported by the National Optical Astronomy Observatory (NOAO). This research draws upon data provided by Dr. Buell Jannuzi and Dr. Arjun Dey as distributed by the NOAO Science Archive. NOAO is operated by AURA, Inc., under a cooperative agreement with the National Science Foundation. This work is based in part on observations made with the Spitzer Space Telescope, which is operated by the Jet Propulsion Laboratory, California Institute of Technology under a contract with NASA.

REFERENCES

Becker, R.H., White R.L. & Helfand, D.J., 1995, AJ, 450, 559

Beckwith, S.V.W. et al. 2006, AJ, 132, 1729

Bell, E.F. et al. 2004, ApJ, 608, 752

Benítez, N. 2000, ApJ, 563, 571

Bertin, E. & Arnouts, S. 1996, A&AS, 117, 393

Bessel, M.S. 1990, PASP, 102, 1181

Blanton, M.R., Brinkmann, J., Csabai, I., Doi, M., Eisenstein, D., Fukugita, M., Gunn, J., Hogg, D. & Schlegel, D. 2003a, AJ, 125, 2348

Blanton, M.R. et al. 2003b, ApJ, 594, 186

Blanton, M.R. & Roweis, S. 2006, submitted (astro-ph/0606170)

Bolzonella, M., Miralles, J.-M. & Pell, R. 2000, A&A, 363, 476

Brodwin, M. et al. 2006, ApJ, in press (astro-ph/0607450)

Brown, M.J.I. et al. 2007, ApJ, 654, 858

Brown, M. et al. in preparation.

Brunner, R.J, Connolly, A.J. & Szalay, A.S. 1999, ApJ, 516, 563

Bruzual,G. Charlot, Stephane 1993ApJ...405..538B

Bruzual, G. & Charlot, S. 2003, MNRAS, 344, 1000

Budavari T., Szalay, A.S., Connolly, A.J., Csabai, I. and Dickinson, M. 2000, AJ, 120, 1588

Coleman, G.D., Wu, C.-C. & Weedman, D.W. 1980, ApJS, 43, 393

Collister, A.A. & Lahav, O. 2004, PASP, 116, 345

Cool, R.J. 2006, ApJS, in press (astro-ph/0611508)

Condon, J.J. et al. 1998, AJ, 115, 1693

Connolly, A.J. et al. 1995, AJ, 110, 2655

Csabai, I., Connolly, A.J., Szalay, A.S. and Budavari, T. 2000, AJ, 119, 69

Csabai, I., et al. 2003, AJ, 125, 580

Devriendt, J.E.G., Guiderdoni, B. & Sadat, R. 1999, A&A, 350, 381

Dey, A. et al. 2005, submitted.

de Vries, W.H. et al. 2002, AJ, 123, 1784

Dickinson, M., Giavalisco, M., and the GOODS Team 2003, *The Great Observatories Origins Deep Survey*, in "The Mass of Galaxies at Low and High Redshift" Proceedings of the ESO Workshop held in Venice, Italy, 24-26 October 2001; eds. R. Bender & A. Renzini, p. 324

Donas, J., Milliard, B. & Laget, M. 1995, A&A, 303, 661

Elston, R.J., Gonzalez, A. H. et al. 2006, ApJ, 639, 816

Eisenhardt, P.R. et al. 2004, ApJS, 154, 48

Eisenstein, D.J. et al. 2007, in preparation

Fabricant, D. et al. 2005, PASP, 117, 1411

Fazio, G.G., et al. 2004, ApJS, 154, 10

Feldmann, R. et al. 2006, MNRAS, in press (astro-ph/0609044)

Fioc, M. & Rocca-Volmerange, B. 1997, A&A, 326, 950

Hogg, D. 1999, astro-ph/9905116

Hogg, D., Baldry, I.K., Blanton, M.R. & Eisenstein, D.J., 2002, astro-ph/0210394

Jannuzi, B. T. & Dey, A. 1999, ASP Conference Series, Vol. 191, p. 111

Jannuzi, B.T. et al. 2005, submitted.

Kauffmann, G. et al. 2003, MNRAS, 341, 33

Kinney, A.L. et al. 1996, ApJ, 1996, 467, 38

Kochanek, C.S. et al. in preparation.

Lawson, C.L. & Hanson, R.J. 1974, *Solving Least Squares Problems*, PrenticeHall.

Lee, K. et al., 2006, ApJ, 642,63

Lin, H., Kirshner, R.P., Shectman, S.A., Landy, S.D., Oemler, A., Tucker, D.L. & Schechter, P. L. 1996, ApJ, 464, 60

Madgwick, D.S. et al. 2003, ApJ, 599, 997

Martin, D.C. et al. 2005, ApJ, 619L, 1

Murray, S.S. et al. 2005, ApJS, 161, 1

Oke, J.B. & Sandage, A. 1968, ApJ, 154, 21

Ouchi, M. et al. 2005, ApJ, 635L, 117

Padmanabhan, T. & Ray, Suryadeep 2006, MNRAS, 372, 53

Schechter, P. 1976, ApJ, 203, 297

Schlegel, D.J., Finkbeiner, D.P. & Davis, M. 1998, ApJ, 500, 525

Schmidt, M. 1968, ApJ, 151, 393

Stern, D. et al. 2005, ApJ, 631, 163

Reach, W.T. et al. 2005, PASP, 117, 978

Rengelink, R.B. et al. 1997, A&A, 124, 259

Scoville N. et al. 2006, ApJS, COSMOS Special Issue

Skrutskie, M.F. et al. 2006,AJ, 131, 1163

Strateva, I. et al. 2001, AJ, 122, 186

Wang, Y., Bahcall, N. & Turner, E.L. 1998, AJ, 116, 2081

Weedman, D.W. et al. 2006, ApJ, 651, 101

Weiner, B.J. et al. 2005, ApJ, 620, 595

White, M. et al. 2007, ApJ, 655L, 69

Wolf, C., Meisenheimer, K., Rix, H.-W., Roch, A., Dye, S., and Kleinheinrich, M. 2003, A&A, 401, 73

York D. et al. 2000, AJ, 120, 1579

Zehavi, I. et al. 2005, ApJ, 630, 1

Table 1. Three Component Spectral Templates

$\lambda(\mu\text{m})$	F_ν ($\times 10^{-14}$ erg/s/cm^2/Hz)		
	E	Sbc	Im
0.1000	0.1086	3.8414	18.6522
0.1029	0.1239	4.8336	23.4179
0.1059	0.1220	4.8676	23.4784
0.1090	0.1267	5.2671	25.1332
0.1122	0.1267	5.3591	25.2659

Note. — Electronic table that presents the flux per unit frequency F_ν of the three components model best fit template spectra as a function of wavelength. Templates are normalized to be at a distance of 10pc and to have an integrated luminosity between the wavelength boundaries of $10^{10} L_\odot$.

Table 2. Four Component Spectral Templates

$\lambda(\mu\mathrm{m})$	F_ν ($\times 10^{-14}$ erg/s/cm^2/Hz)			
	E	Sbc	Im	E+A
0.1000	0.1430	3.5994	27.7314	0.0822
0.1029	0.1632	4.5298	34.8230	0.0942
0.1059	0.1604	4.5628	34.9195	0.0929
0.1090	0.1670	4.9381	37.3873	0.1383
0.1122	0.1665	5.0253	37.5922	0.1935

Note. — Electronic table that presents the flux per unit frequency F_ν of the four components model best fit template spectra as a function of wavelength. Templates are normalized to be at a distance of 10pc and to have an integrated luminosity between the wavelength boundaries of $10^{10} L_\odot$.

Table 3. Three Template Model Absolute Magnitudes

z	Template	B_w	B	V	R	I	u’	g’	r’	i’	z’	J	H	K_s	K	C1	C2	C3	C4	DM
0.0	1	−18.47	−18.57	−19.49	−20.14	−20.82	−17.03	−18.97	−19.78	−20.20	−20.57	−21.68	−22.49	−22.66	−22.63	−22.99	−22.84	−22.81	−22.00	
0.0	2	−17.96	−17.99	−18.61	−19.29	−19.90	−17.20	−18.25	−18.94	−19.30	−19.70	−21.00	−21.94	−22.36	−22.35	−23.29	−23.44	−25.39	−27.40	
0.0	3	−19.34	−19.35	−19.72	−20.11	−20.40	−18.78	−19.56	−19.85	−19.92	−20.02	−20.82	−21.36	−21.49	−21.47	−21.93	−21.94	−23.67	−25.31	
0.1	1	−17.89	−18.06	−19.32	−20.02	−20.73	−16.41	−18.64	−19.66	−20.10	−20.50	−21.77	−22.47	−22.88	−22.88	−23.18	−23.20	−23.18	−22.53	38.32
0.1	2	−17.70	−17.74	−18.51	−19.16	−19.85	−17.09	−18.11	−18.76	−19.28	−19.58	−21.04	−21.85	−22.55	−22.56	−23.42	−23.59	−24.39	−27.28	38.32
0.1	3	−19.21	−19.23	−19.77	−20.11	−20.50	−18.57	−19.49	−19.83	−20.02	−20.07	−20.95	−21.48	−21.71	−21.71	−22.19	−22.16	−22.75	−25.34	38.32
0.2	1	−17.20	−17.50	−19.12	−19.89	−20.64	−15.53	−18.16	−19.50	−20.01	−20.42	−21.82	−22.45	−23.11	−23.11	−23.36	−23.50	−23.43	−23.10	39.96
0.2	2	−17.42	−17.47	−18.44	−19.03	−19.80	−17.07	−17.88	−18.65	−19.17	−19.53	−21.04	−21.81	−22.68	−22.70	−23.37	−23.79	−24.20	−26.92	39.96
0.2	3	−18.99	−19.01	−19.74	−20.15	−20.58	−18.51	−19.37	−19.87	−20.07	−20.16	−21.07	−21.56	−21.93	−21.93	−22.30	−22.40	−22.64	−25.07	39.96
0.3	1	−16.71	−16.95	−18.77	−19.75	−20.55	−14.47	−17.60	−19.33	−19.92	−20.34	−21.79	−22.51	−23.25	−23.26	−23.50	−23.69	−23.68	−23.56	40.96
0.3	2	−17.28	−17.29	−18.30	−18.95	−19.70	−17.02	−17.64	−18.59	−19.02	−19.51	−20.97	−21.84	−22.71	−22.75	−23.39	−23.98	−24.23	−26.41	40.96
0.3	3	−18.76	−18.82	−19.70	−20.15	−20.60	−18.43	−19.19	−19.89	−20.04	−20.24	−21.15	−21.64	−22.10	−22.11	−22.44	−22.65	−22.74	−24.65	40.96

Note. — The electronic table supplies the absolute magnitude of the three template model as a function of redshift, along with the distance modulus DM. A complete version of this table can be found in the electronic edition of the journal. The absolute magnitude we present here corresponds to the canonical definition of the absolute magnitude (as in, for example, eqn. 26 of Hogg 1999) plus the K correction term. This allows the calculation of photometric redshifts and K corrections from the table. To determine photometric redshifts, colors should be calculated and matched to the data by varying the a_k coefficients (see § 3.1) and the redshift. For a galaxy at redshift z with template coefficients a_k, the model magnitude in band b is given by $M_b(z) = -2.5 \log \sum_k a_k 10^{-0.4 M_{b,k}(z)}$. Apparent magnitudes can be determined by adding the distance modulus to the absolute ones. To determine K corrections for a galaxy at redshift z, coefficients a_k should also be determined to match the observed colors as above. With the same coefficients, redshift z and redshift zero model absolute magnitudes can be determined, and the difference between them will correspond to the desired K correction.

Table 4. Four Template Model Absolute Magnitudes

z	Template	B_w	B	V	R	I	u’	g’	r’	i’	z’	J	H	K_s	K	C1	C2	C3	C4	DM
0.0	1	–18.29	–18.41	–19.45	–20.11	–20.81	–16.86	–18.87	–19.74	–20.19	–20.57	–21.73	–22.52	–22.73	–22.70	–23.00	–22.80	–22.69	–22.32	
0.0	2	–18.09	–18.13	–18.78	–19.46	–20.06	–17.15	–18.40	–19.12	–19.46	–19.86	–21.12	–22.09	–22.49	–22.48	–23.36	–23.53	–25.37	–27.17	
0.0	3	–18.87	–18.86	–19.23	–19.62	–19.99	–18.49	–19.08	–19.35	–19.47	–19.67	–20.61	–21.28	–21.53	–21.50	–22.16	–22.07	–24.28	–26.63	
0.0	4	–19.68	–19.70	–20.04	–20.43	–20.70	–18.69	–19.87	–20.18	–20.22	–20.29	–21.07	–21.58	–21.79	–21.76	–22.22	–22.35	–23.08	–23.77	
0.1	1	–17.65	–17.85	–19.27	–19.99	–20.71	–16.33	–18.47	–19.62	–20.07	–20.49	–21.79	–22.51	–22.91	–22.92	–23.20	–23.19	–23.10	–22.62	38.32
0.1	2	–17.78	–17.85	–18.66	–19.33	–20.01	–16.84	–18.24	–18.93	–19.45	–19.73	–21.14	–22.01	–22.64	–22.66	–23.50	–23.69	–24.45	–27.17	38.32
0.1	3	–18.79	–18.79	–19.29	–19.62	–20.04	–18.37	–19.01	–19.33	–19.54	–19.67	–20.72	–21.32	–21.75	–21.76	–22.35	–22.29	–23.10	–26.54	38.32
0.1	4	–19.44	–19.49	–20.04	–20.45	–20.80	–18.25	–19.81	–20.17	–20.33	–20.36	–21.20	–21.64	–21.96	–21.98	–22.46	–22.52	–23.08	–23.88	38.32
0.2	1	–17.02	–17.29	–18.99	–19.85	–20.61	–15.55	–17.93	–19.46	–19.97	–20.41	–21.82	–22.50	–23.13	–23.12	–23.39	–23.51	–23.37	–23.05	39.96
0.2	2	–17.37	–17.49	–18.57	–19.20	–19.97	–16.75	–17.97	–18.80	–19.35	–19.69	–21.16	–21.96	–22.79	–22.80	–23.48	–23.88	–24.28	–26.85	39.96
0.2	3	–18.68	–18.66	–19.24	–19.67	–20.09	–18.37	–18.93	–19.39	–19.56	–19.70	–20.81	–21.36	–21.93	–21.94	–22.36	–22.61	–22.85	–26.10	39.96
0.2	4	–18.97	–19.10	–20.07	–20.44	–20.89	–17.85	–19.62	–20.15	–20.39	–20.46	–21.32	–21.74	–22.17	–22.18	–22.62	–22.73	–23.08	–23.98	39.96
0.3	1	–16.61	–16.80	–18.56	–19.69	–20.51	–14.61	–17.38	–19.25	–19.88	–20.31	–21.79	–22.55	–23.27	–23.28	–23.54	–23.71	–23.65	–23.46	40.96
0.3	2	–17.08	–17.16	–18.43	–19.10	–19.88	–16.73	–17.64	–18.73	–19.20	–19.68	–21.12	–21.96	–22.85	–22.89	–23.52	–24.05	–24.32	–26.36	40.96
0.3	3	–18.55	–18.56	–19.20	–19.67	–20.10	–18.40	–18.85	–19.41	–19.54	–19.76	–20.84	–21.43	–22.03	–22.05	–22.45	–22.87	–22.87	–25.39	40.96
0.3	4	–18.46	–18.68	–20.07	–20.45	–20.93	–17.48	–19.29	–20.16	–20.39	–20.55	–21.40	–21.87	–22.33	–22.33	–22.69	–22.94	–23.14	–24.05	40.96

Note. — The electronic table supplies the absolute magnitude of the four template model as a function of redshift, along with the distance modulus DM. A complete version of this tables can be found on the electronic edition of the journal. See the caption of Table 3 for directions on how use the tables to determine photometric redshifts and K corrections.

Table 5. Photometric - Spectroscopic Redshift Comparison Summary

Templates and Sample	$\sigma_z/(1+z)$	Δz	68.3%	95.5%	99.7%	Median
3 template/complete sample	0.060	0.038	0.039	0.126	0.348	0.016
3 template/χ^2 limited	0.044	0.030	0.033	0.088	0.245	0.020
4 template/complete sample	0.060	0.039	0.042	0.119	0.335	0.014
4 template/χ^2 limited	0.048	0.033	0.037	0.092	0.268	0.023

Note. — Summary of the photometric redshifts calculations for the AGES photometric galaxy sample. For each case discussed in § 4.3 we present $\sigma_z/(1+z)$ (as defined in eq. [14]), Δz (the 95% clipped distribution $\sigma_z/(1+z)$), the ranges of $|z_p - z_s|/(1+z_s)$ encompassing 68.3, 95.5 and 99.7% of the distribution and the median value of $z_p - z_s$.

Table 6. NDWFS Boötes Field B-band Luminosity Functions

$\hat{e}$ range	z range	$M^* - 5\log h$	α	$\phi^*(h^3\ \mathrm{Mpc}^{-3}\ \mathrm{mag}^{-1})$
$0.8 < \hat{e} < 1.0$	$0.0 < z < 0.2$	-18.99 ± 0.12	0.22 ± 0.16	$8.95 \pm 0.38 \times 10^{-3}$
	$0.2 < z < 0.4$	-19.48 ± 0.07	0.21 ± 0.10	$4.35 \pm 0.11 \times 10^{-3}$
	$0.4 < z < 0.6$	-19.68 ± 0.02	0.21 ± 0.00	$3.86 \pm 0.07 \times 10^{-3}$
	$0.6 < z < 0.8$	-19.73 ± 0.03	0.21 ± 0.00	$2.15 \pm 0.08 \times 10^{-3}$
$0.4 < \hat{e} < 0.8$	$0.0 < z < 0.2$	-19.00 ± 0.17	-0.64 ± 0.19	$8.69 \pm 1.28 \times 10^{-3}$
	$0.2 < z < 0.4$	-19.45 ± 0.08	-0.23 ± 0.10	$5.19 \pm 0.22 \times 10^{-3}$
	$0.4 < z < 0.6$	-19.71 ± 0.02	-0.23 ± 0.00	$5.33 \pm 0.10 \times 10^{-3}$
	$0.6 < z < 0.8$	-19.73 ± 0.02	-0.23 ± 0.00	$4.64 \pm 0.16 \times 10^{-3}$
$0.0 < \hat{e} < 0.4$	$0.0 < z < 0.2$	-18.86 ± 0.07	-1.30 ± 0.02	$13.85 \pm 1.07 \times 10^{-3}$
	$0.2 < z < 0.4$	-19.22 ± 0.08	-0.67 ± 0.11	$11.00 \pm 0.71 \times 10^{-3}$
	$0.4 < z < 0.6$	-19.72 ± 0.02	-0.67 ± 0.00	$9.14 \pm 0.19 \times 10^{-3}$
	$0.6 < z < 0.8$	-19.79 ± 0.02	-0.67 ± 0.00	$9.26 \pm 0.34 \times 10^{-3}$
$0.0 < \hat{e} < 1.0$	$0.0 < z < 0.2$	-19.64 ± 0.05	-1.23 ± 0.02	$15.59 \pm 0.86 \times 10^{-3}$
	$0.2 < z < 0.4$	-19.55 ± 0.05	-0.54 ± 0.06	$18.07 \pm 0.67 \times 10^{-3}$
	$0.4 < z < 0.6$	-19.87 ± 0.01	-0.54 ± 0.00	$17.13 \pm 0.21 \times 10^{-3}$
	$0.6 < z < 0.8$	-20.00 ± 0.01	-0.54 ± 0.00	$12.10 \pm 0.25 \times 10^{-3}$

Note. — Best fit Schechter function parameters for the luminosity functions of the NDWFS Boötes field.

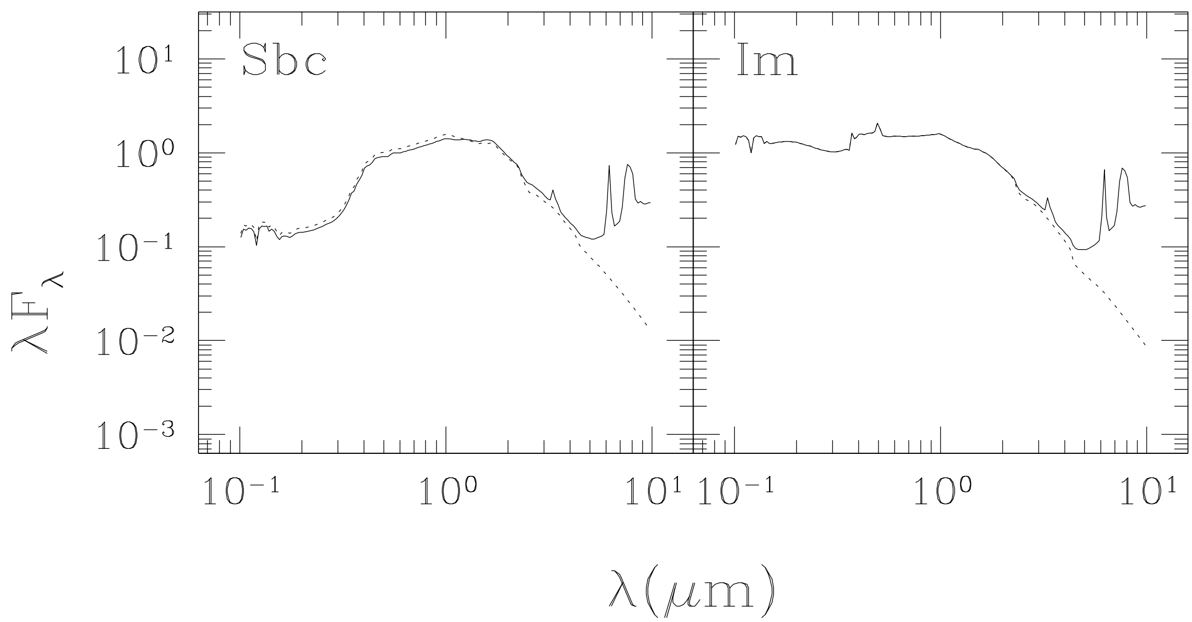

Fig. 1.— The solid lines show our initial guesses for the Sbc (left) and Im (right) templates, which were generated by extending the CWW templates to the mid-IR with the Bruzual & Charlot (2003) synthetic models and then adding the mid-IR part of the M82 and VCC 1003 templates of Devriendt, Guiderdoni & Sadat (1999) to include dust/PAH emission features. For comparison, the dashed lines show the CWW templates extended into the mid-IR based only on the Bruzual & Charlot (2003) models.

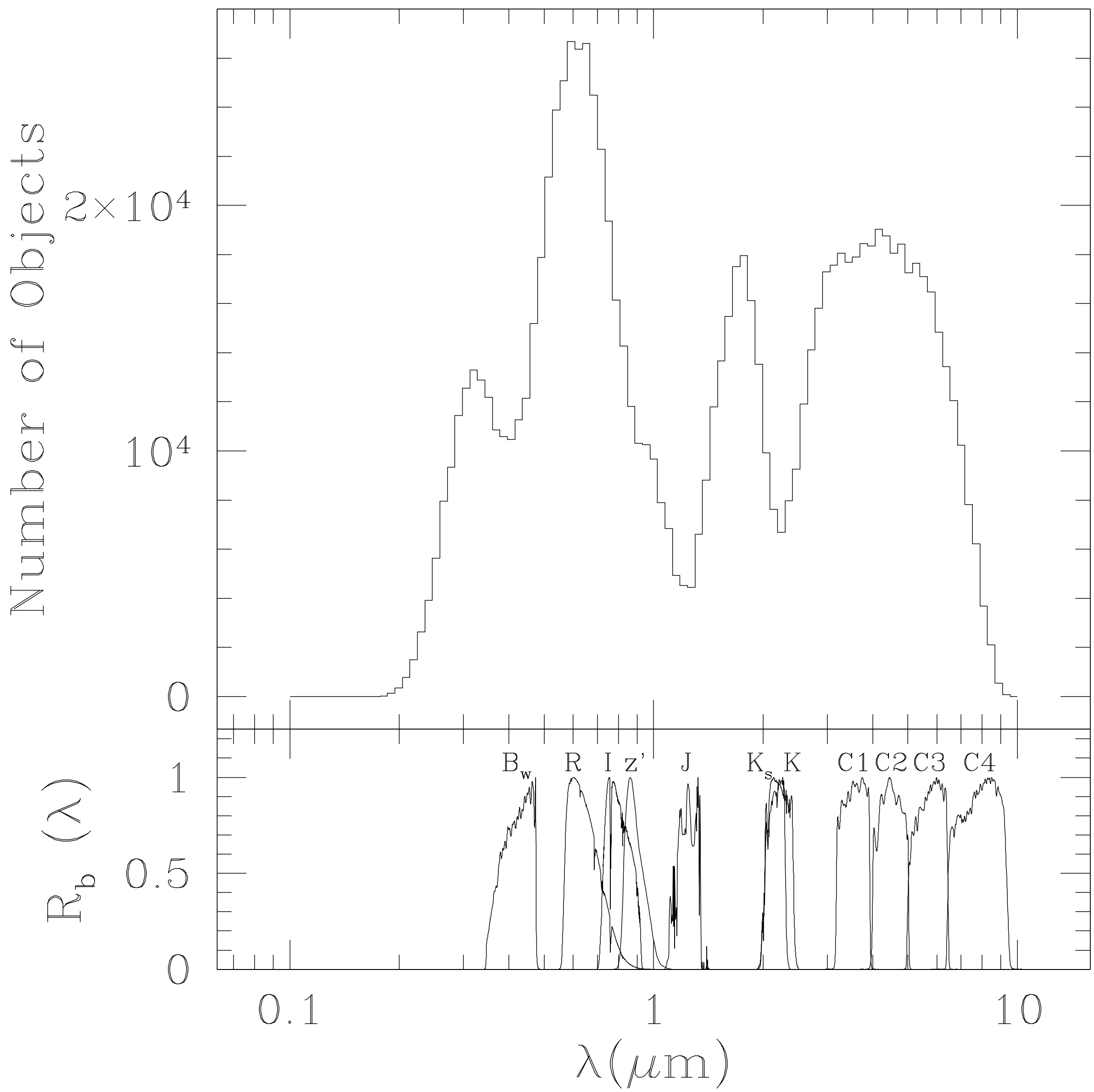

Fig. 2.— *(Top panel)* The number of measurements used to derive the templates as a function of wavelength. We consider object i to contribute to wavelength bin n if S_{i,b,λ_n} (as defined in eqn. [4]) is at least 10% of its maximum in band b. *(Bottom panel)* Filter sensitivity curves for the AGES bands. The dips seen in the top panel near 0.4, 1.2 and 2.1 μm are caused by the lack of V and H-band data and the significant gap between K and C1.

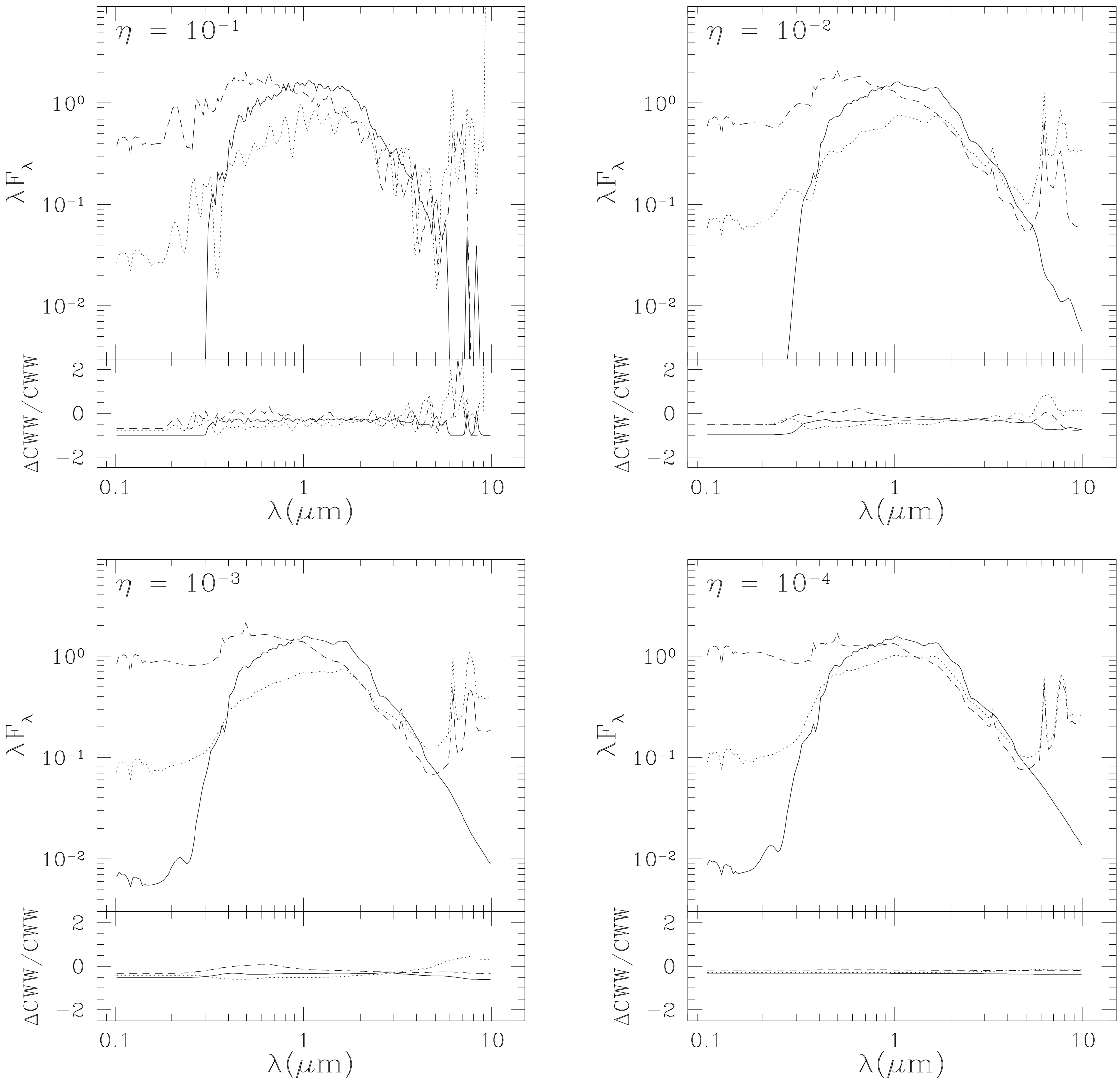

Fig. 3.— *(Top sub-panels)* The Elliptical (solid line), Sbc (dotted) and Im (dashed) templates as a function of the smoothing strength weight η. Lower values of η correspond to stronger smoothing. *(Bottom sub-panels)* The fractional change in the templates from the extended-CWW templates. For each case, we have approximately 90600 degrees of freedom.

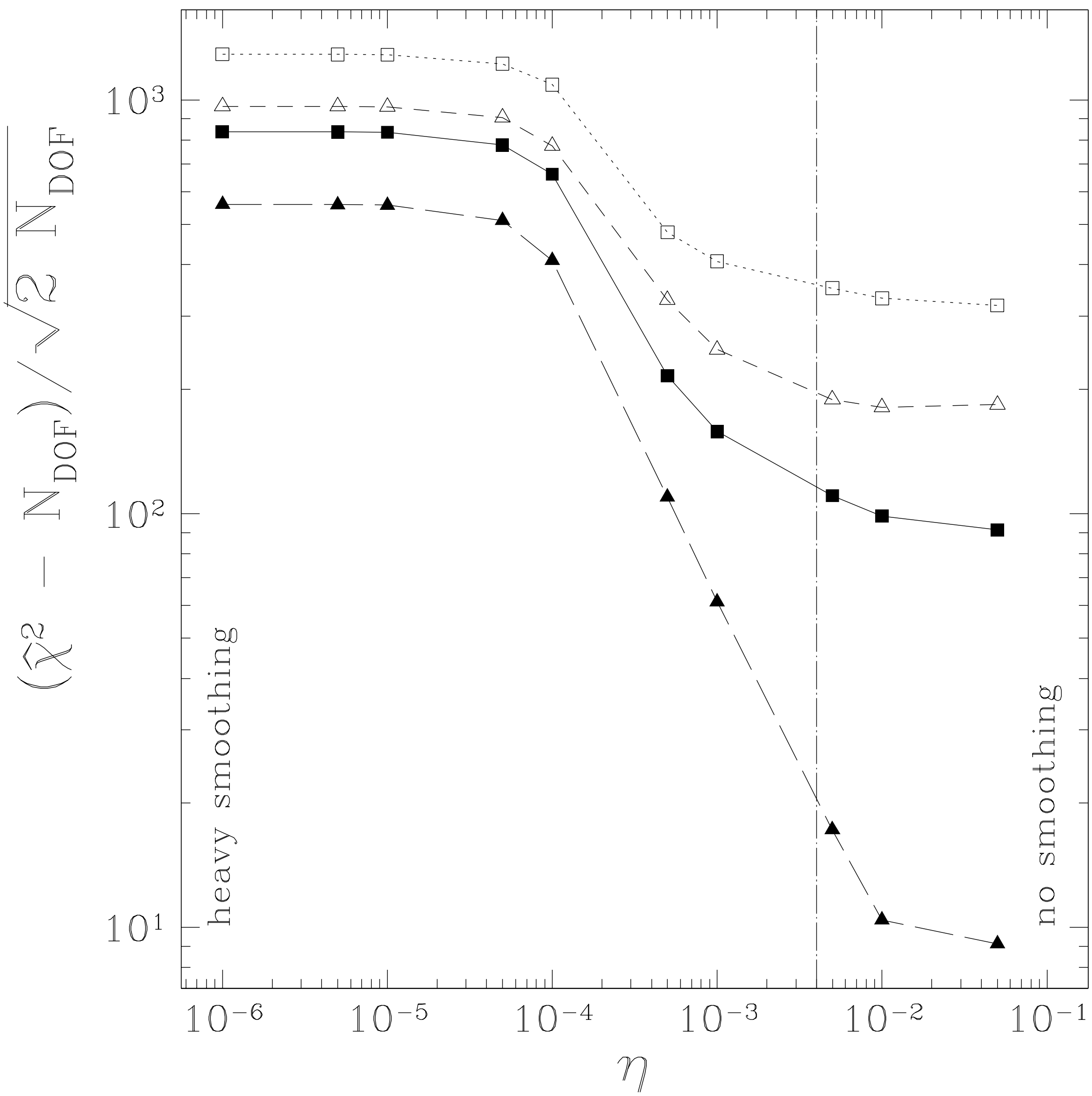

Fig. 4.— The deviation of the goodness of fit χ^2 from the number of degrees of freedom $N_{\rm DOF}$ in units of the expected standard deviation in the absence of smoothing, $\sqrt{2\rm N_{DOF}}$, as a function of the smoothing strength parameter η for the three *(squares)* and four *(triangle)* template models. The selected value of $\eta = 0.004$ is indicated by the vertical line. In the plot, $\hat{\chi}^2$ stands for the normalized χ^2 such that if $\eta \rightarrow \infty$, $\hat{\chi}^2 = \rm N_{DOF}$ for the four template model. The filled points show the results for the subsample used to build the templates, where we drop the 3% of galaxies with the worst fit, and the open points show the results including all objects. That those 3% of galaxies contribute more than 70% of the total χ^2 justifies their elimination.

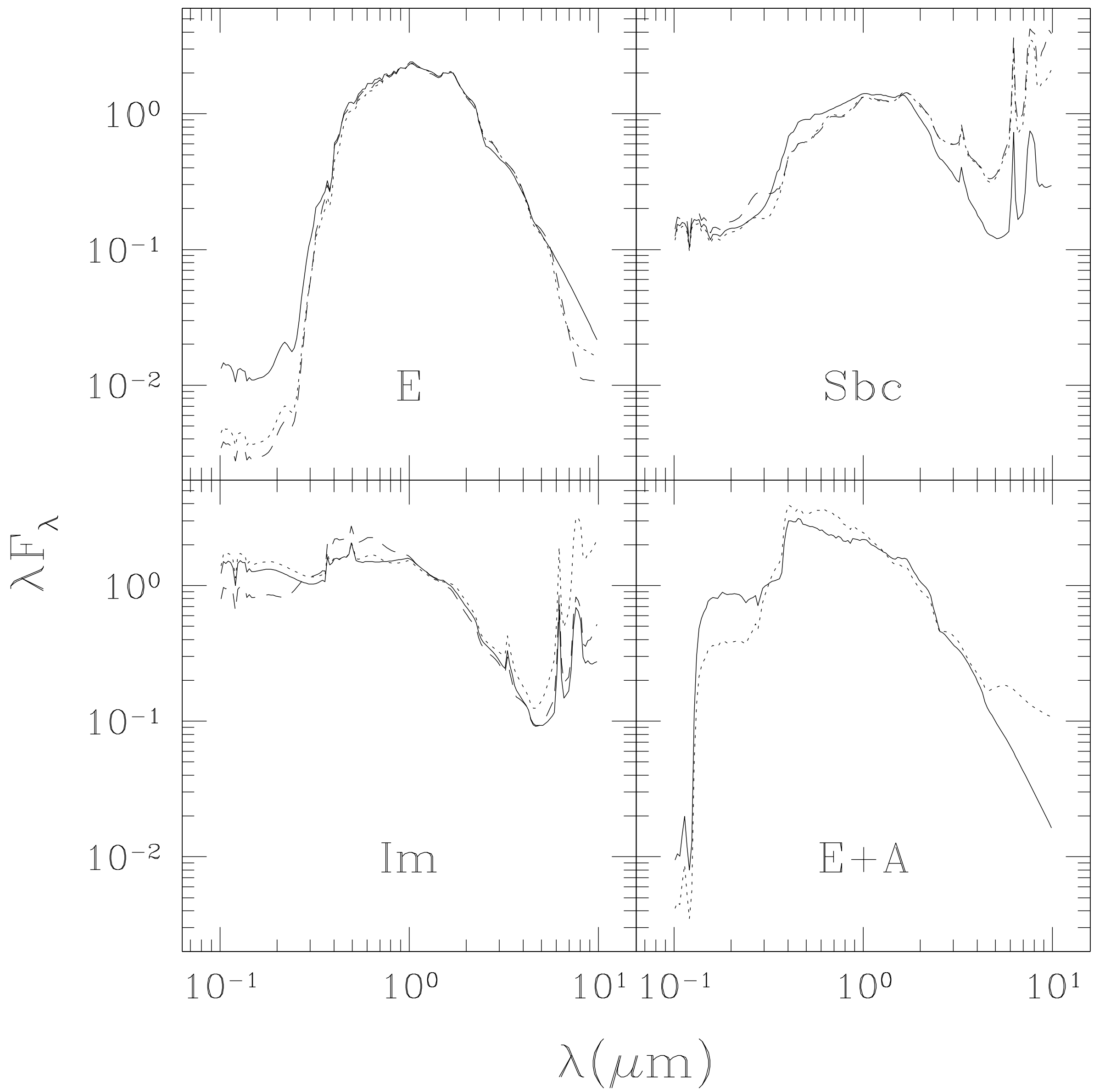

Fig. 5.— The templates derived using the algorithm described in § 3.1 for the three *(dashed)* and four *(dotted)* template models compared to their initial guesses *(solid)*. All templates are normalized so that they have the same integrated energy from 0.5 to 2μm.

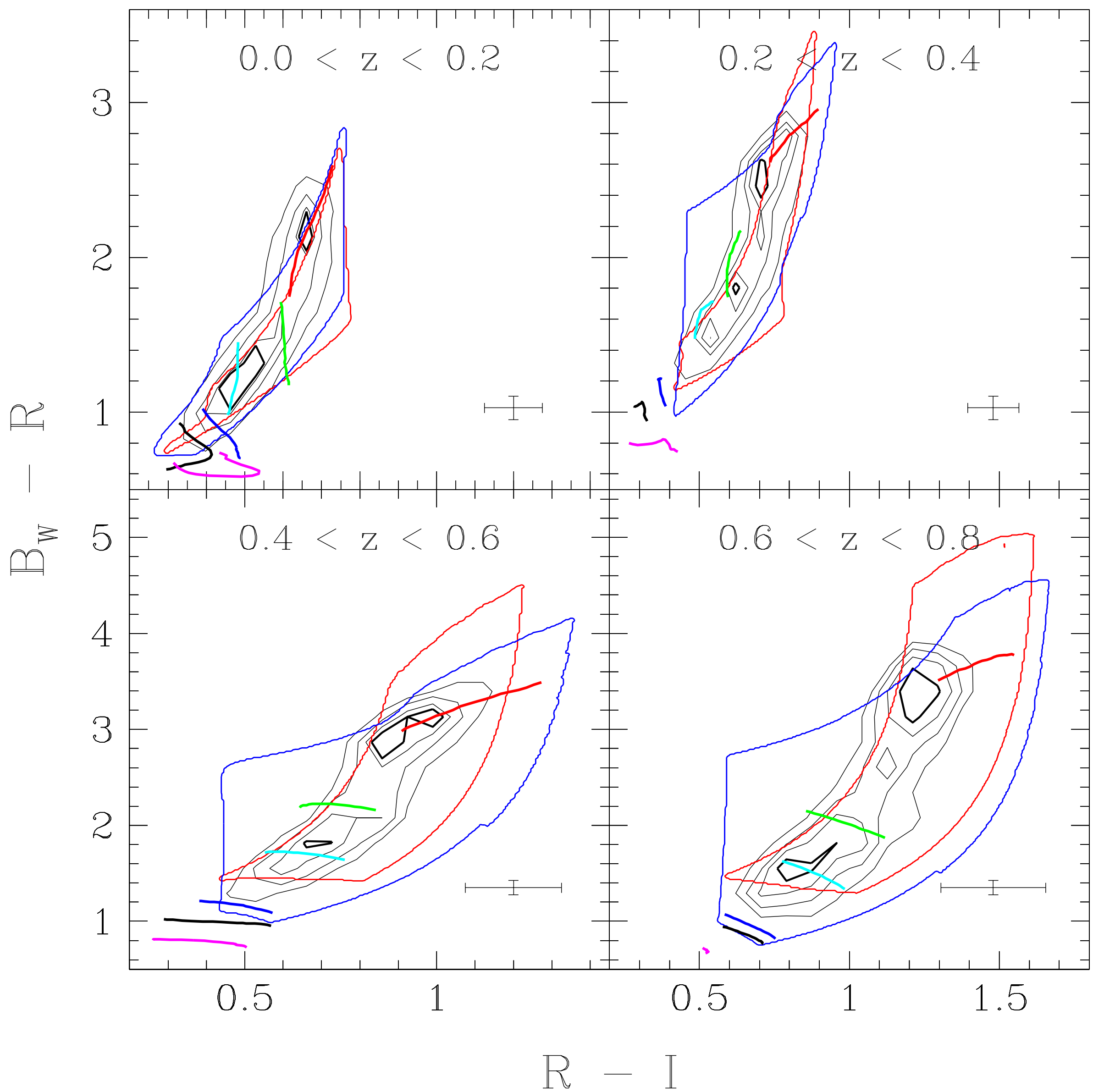

Fig. 6.— The color–color distributions of the AGES galaxy sample for four different redshift ranges in the optical bands. The black contours enclose 20 (bold), 40, 60 and 80% of the galaxies in the sample. Solid lines mark the borders of the areas covered by our three *(red)* and four *(blue)* template models. The error bars in the bottom right of each panel show the typical color error for galaxies in each sample. For comparison we show in thick lines the colors of six common templates from the literature: CWW Elliptical *(red)*, Sbc *(green)*, Scd *(cyan)* and Im *(blue)*, and Kinney et al. (1996) SB1 *(yellow)* and SB2 *(magenta)*.

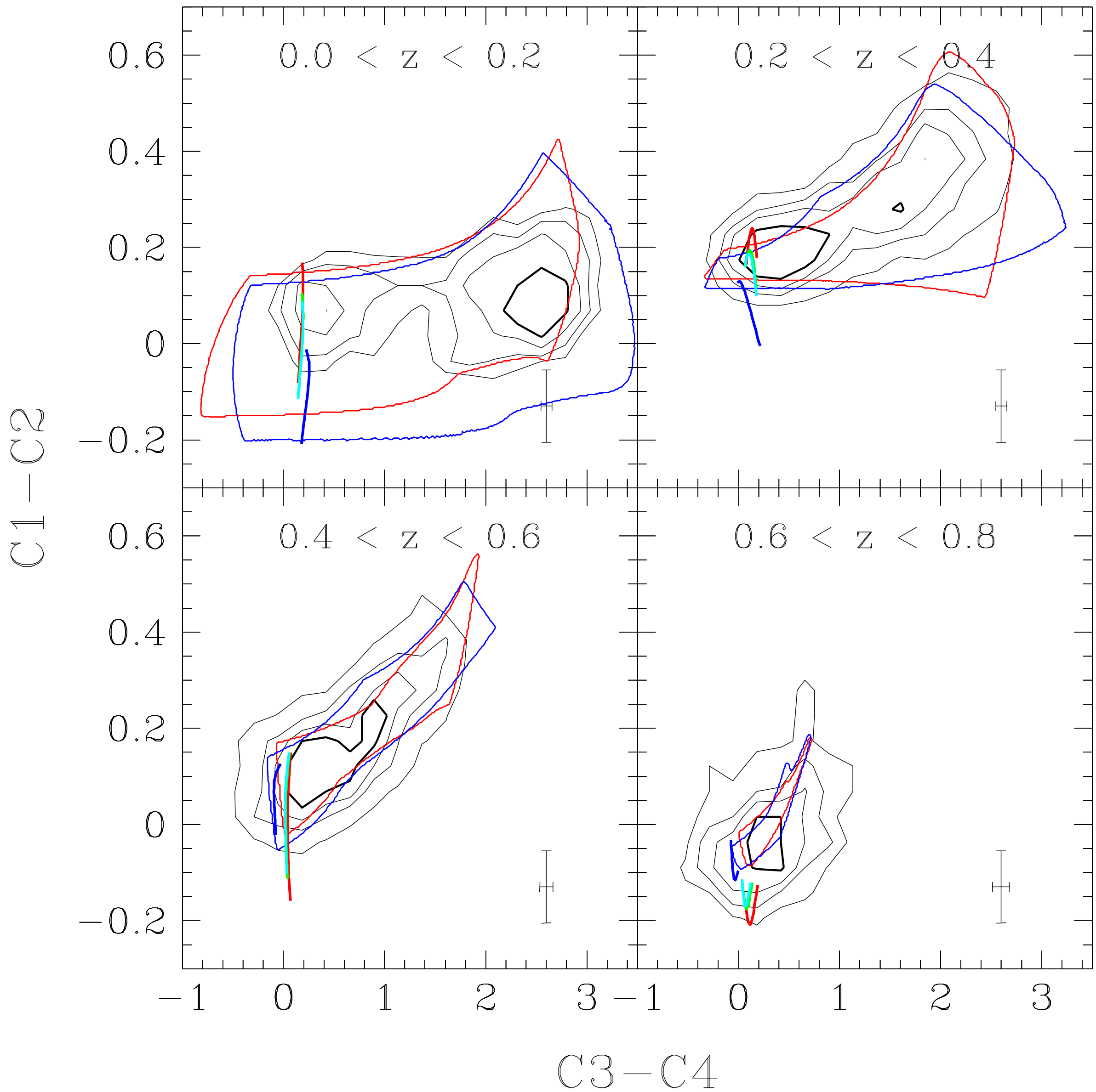

Fig. 7.— The color–color distributions of the AGES galaxy sample for four different redshift ranges in the mid-IR bands. Contours are defined in the same way as in Fig. 6. For comparison, we show the Bruzual & Charlot (2003) extended CWW templates in the same color-coding as in the optical. Notice that the E, Sbc and Scd colors sometimes overlap since they are very similar in this wavelength range. Also note that the low redshift galaxy distribution is strongly bimodal.

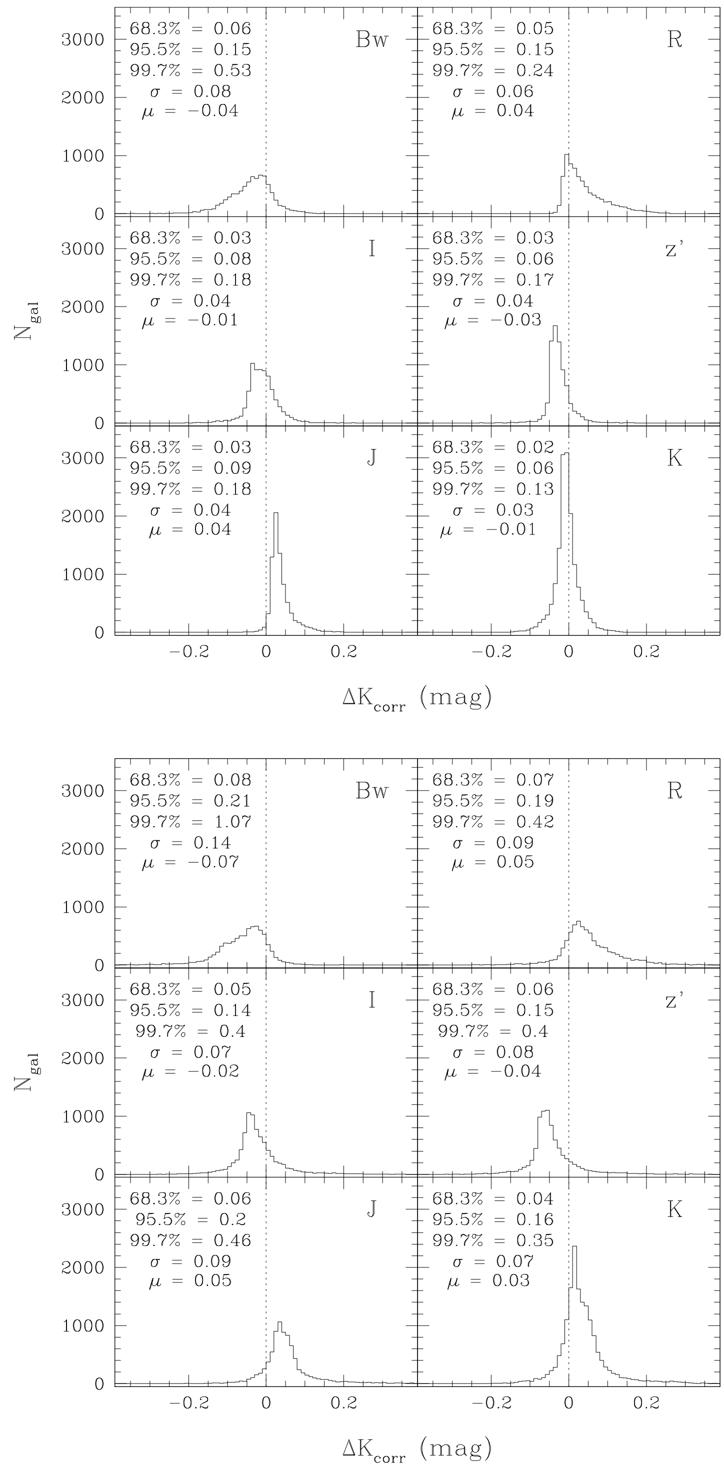

Fig. 8.— Histograms of the differences between the K corrections determined here and those determined by `kcorrect v4_1_4` of Blanton et al. (2003a) for the AGES galaxy sample in all optical and near-IR AGES bands (K and K_s have been combined into a single K band) for redshifts lower *(top)* and higher *(bottom)* than 0.3. Each panel also gives the standard deviation between the methods σ, the mean μ of ΔK_{corr} and the values of $|\Delta K_{corr}|$ that encompasses 68.3, 95.5 and 99.7% of the objects. The IRAC bands are not considered since `kcorrect v4_1_4` cannot model mid-IR fluxes.

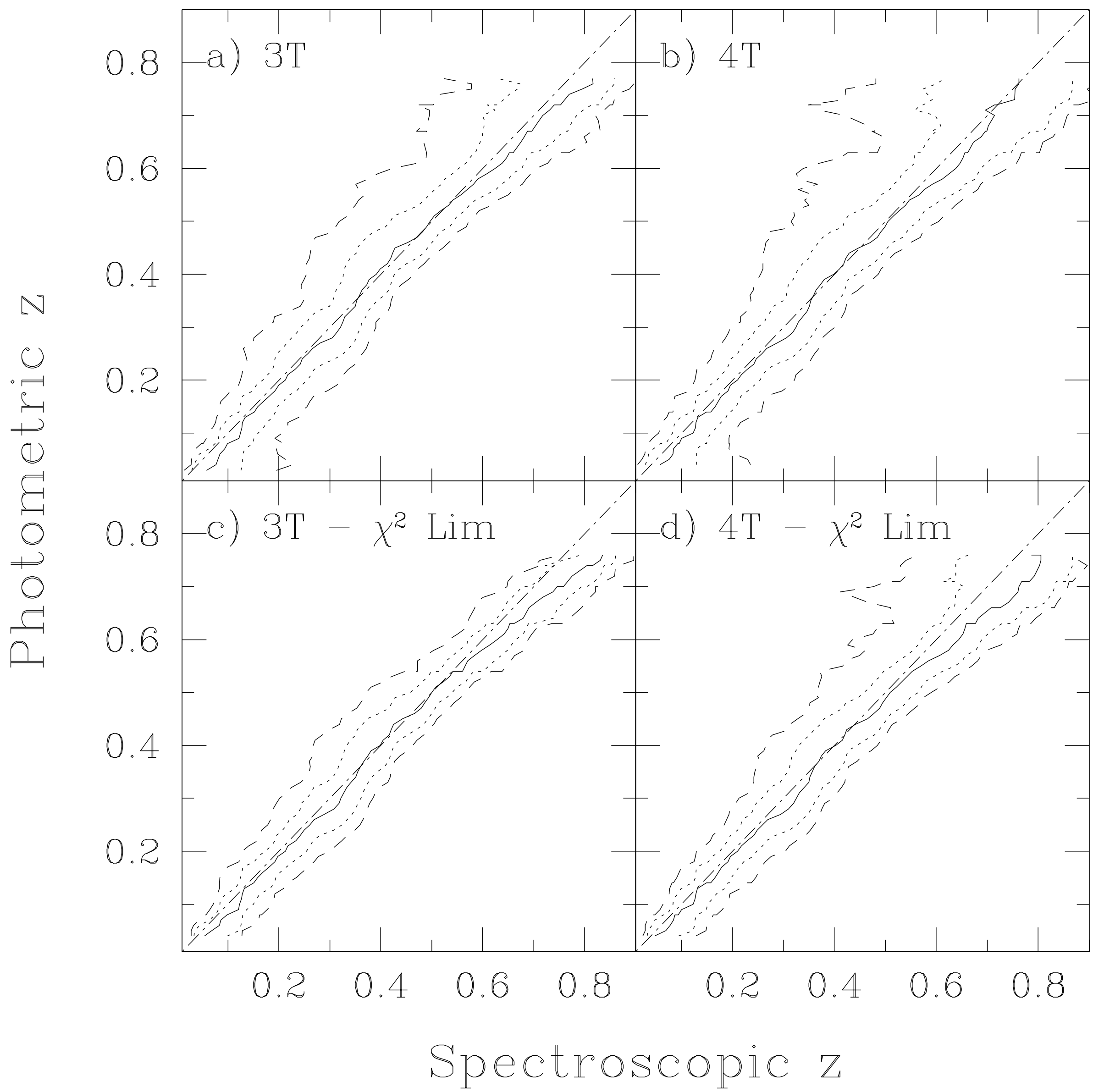

Fig. 9.— Comparison of photometric and spectroscopic redshifts. For a fixed photometric redshift, the solid line shows the median of the spectroscopic redshifts, while the dotted and dashed lines contain the 68.3 and 90% of the distribution respectively. The two redshifts are equal, $z_p = z_s$, on the diagonal dot dashed line. Panel *a*) shows the comparison for the 3 template model and *b*) for the 4 template one. For the bottom panels, *c*) and *d*), we have only included the 75% of the objects for which there is a probability greater than 10% of obtaining a χ^2 larger than that of the best fit.

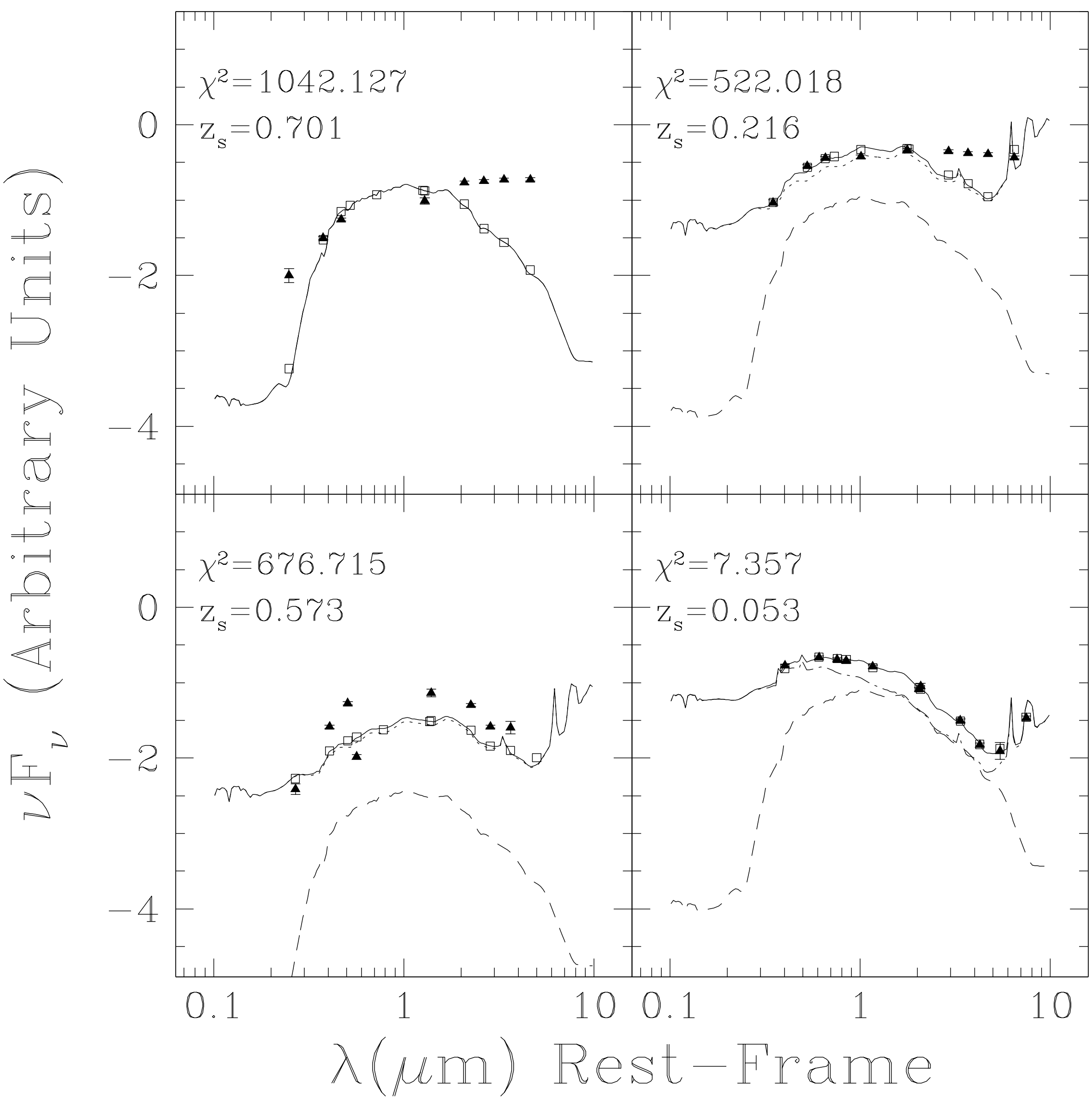

Fig. 10.— Examples of bad and good fits to the data. In each panel we show the photometric data *(triangles)*, the model bandpass fluxes *(squares)*, the overall model SED *(solid line)* and the E *(dashed line)*, Sbc *(dotted line)* and Im *(dot-dashed line)* contributions to the model SED. The top panels show the fit for galaxies with AGN contamination. The bottom left panel is a galaxy with bad photometry in the z' band. Finally, the bottom right panel shows the median fit for comparison.

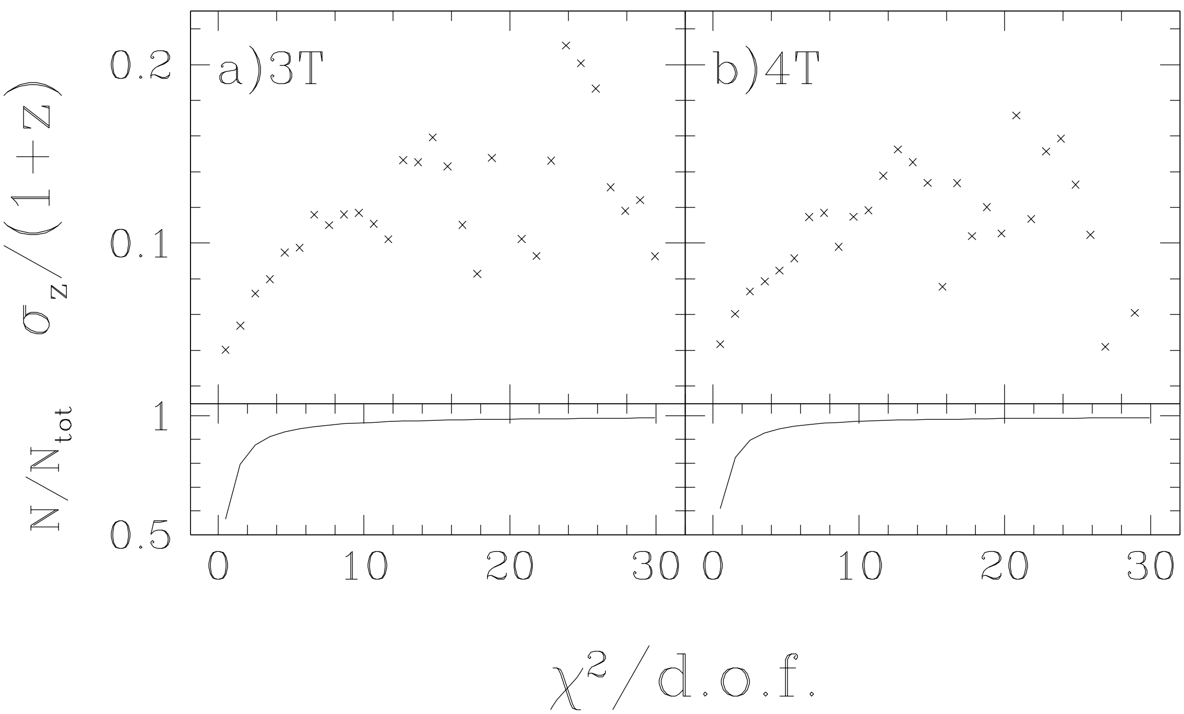

Fig. 11.— *(Top)* The dispersion $\sigma_z/(1+z)$ defined in equation (14) as a function of the χ^2 per degree of freedom for the fits to the photometry at the best photometric redshift in the three *(left)* and four *(right)* template models. The points are the mean values for objects divided in bins with a width of one unit of χ^2 per degree of freedom. *(Bottom)* The fraction of objects with fits better than that $\chi^2/N_{\rm DOF}$. The correlation between χ^2 and $\sigma_z/(1+z)$ justifies the χ^2 cut used in the bottom panel of Figure 9.

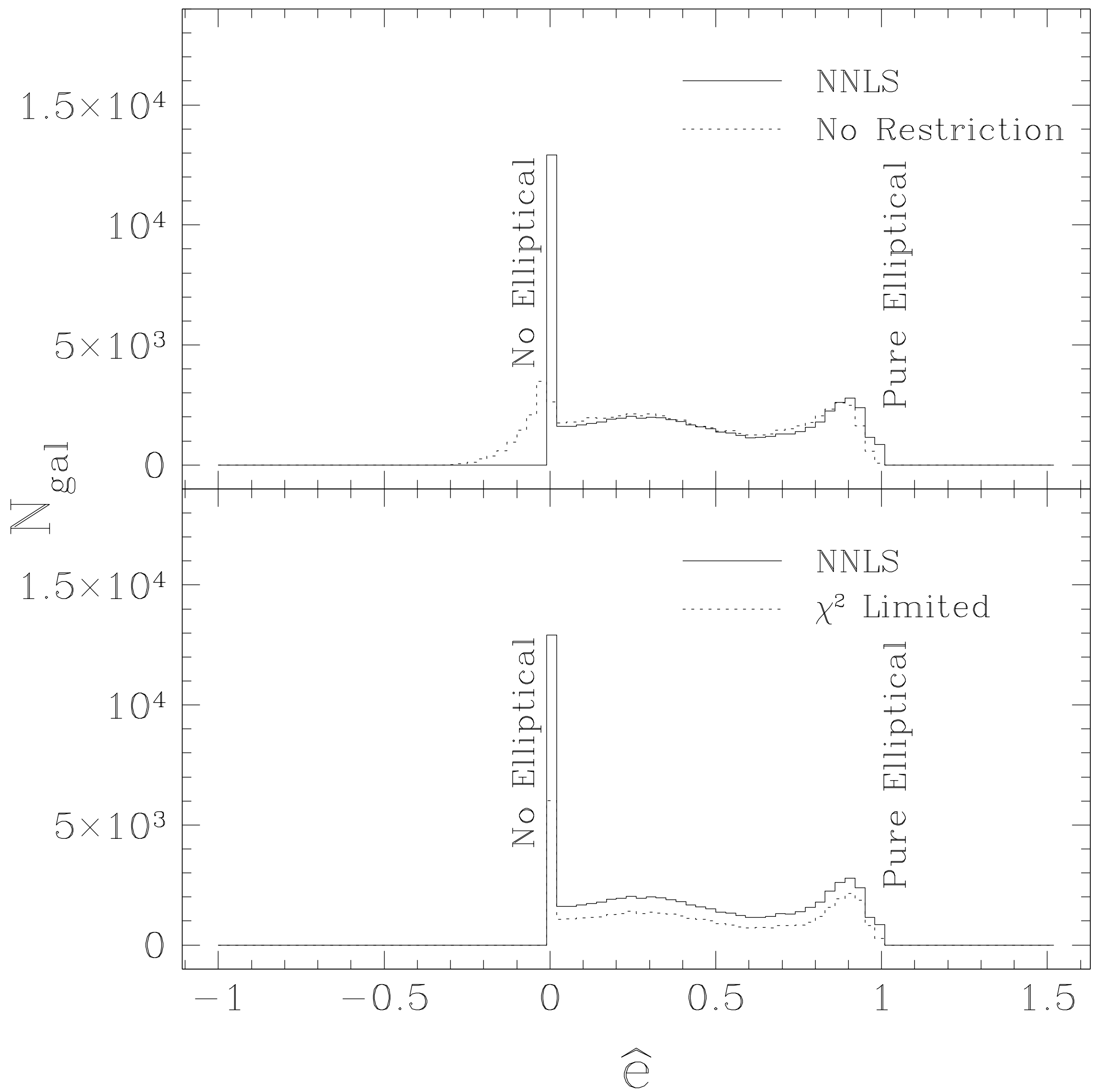

Fig. 12.— Distribution of galaxies as a function of the elliptical component fraction $\hat{e}$ in their SED. In both panels, the bold solid line shows the distribution obtained using the NNLS algorithm to enforce $a_k \geq 0$. The dotted line in the top panel shows the distribution when we drop this restriction, while in the bottom panel it shows the distribution when using the NNLS algorithm but applying the χ^2 cut of § 4.3.

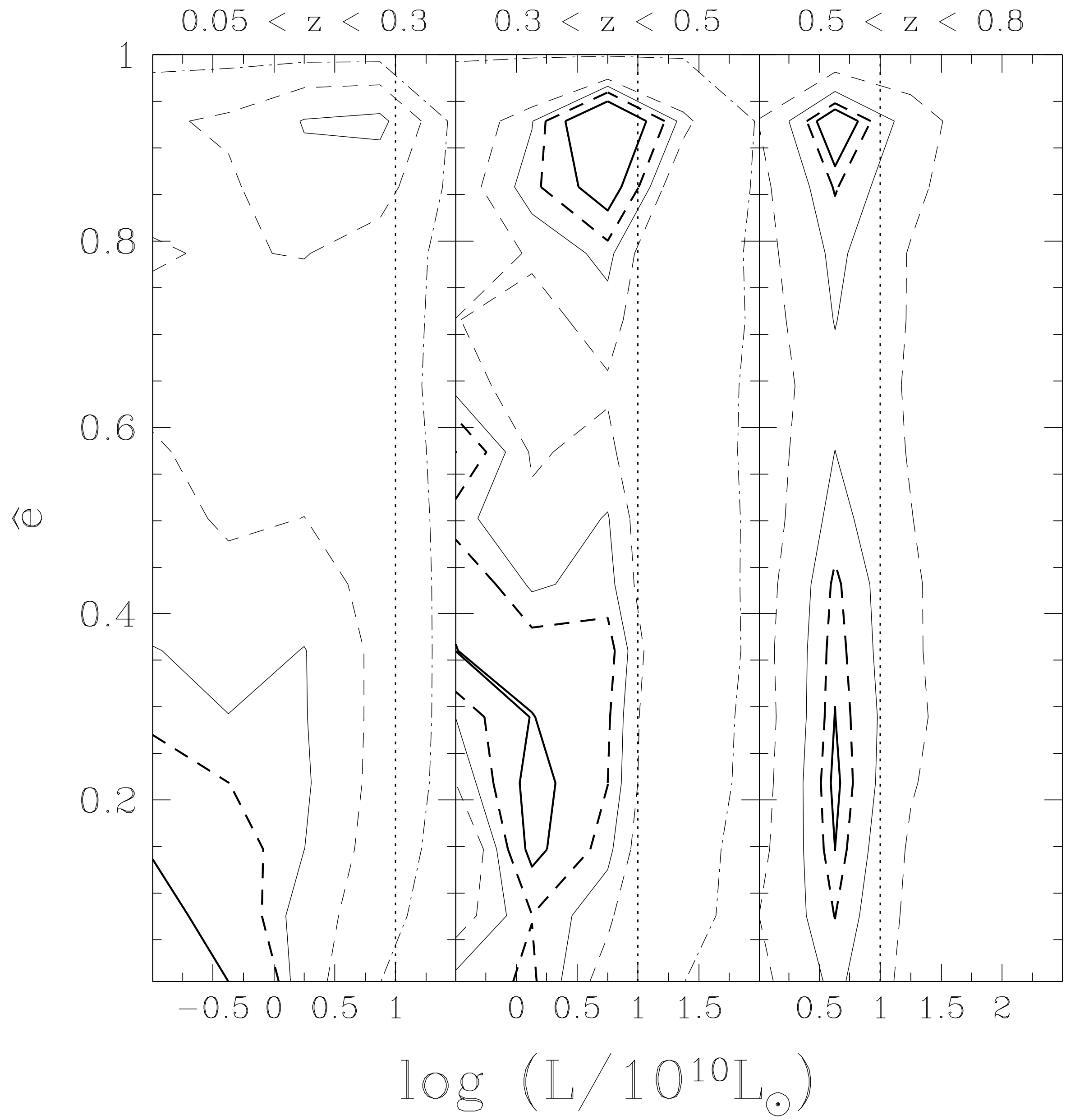

Fig. 13.— Contour plots of the distribution of galaxies as a function of their bolometric luminosity and the amount of elliptical component in their SEDs for three redshift ranges. The contour levels, with the ordering of bold solid, bold dashed, thin solid, thin dashed and thin dot-dashed, enclose 20%,40%,60% and 100% of the objects respectively. The vertical dotted line shows $\log L/10^{10}L_\odot = 1$. In each redshift range we see a bimodal distribution of galaxies with either high or low star formation rates.

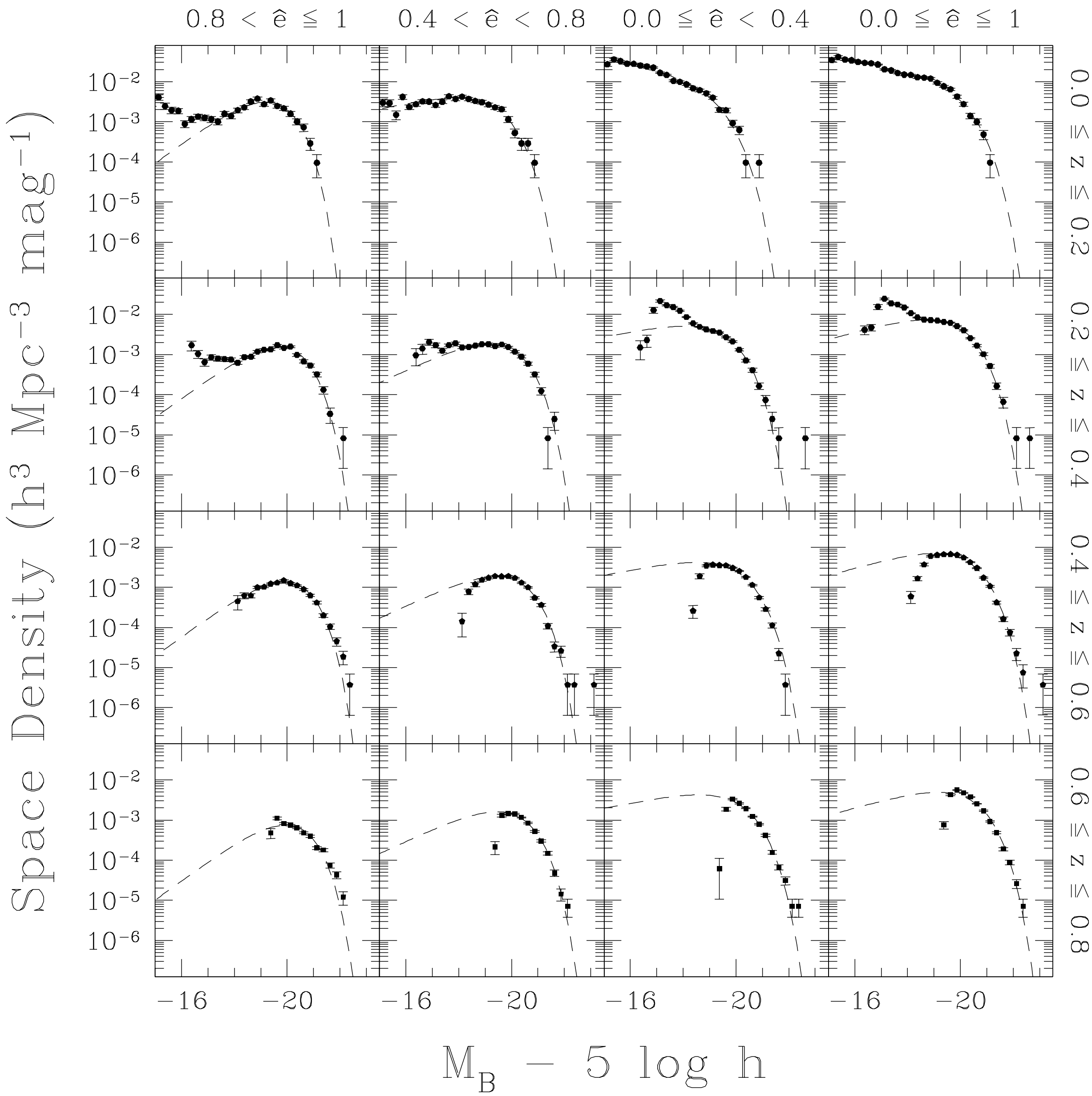

Fig. 14.— Luminosity functions for the NDWFS Boötes field. They are divided into three $\hat{e}$ ranges 1–0.8 *(left)*, 0.8–0.4 *(middle-left)* and 0.4–0.0 *(middle-right)*, and into four redshift ranges 0.0–0.2 *(top)*, 0.2–0.4 *(middle-top)*, 0.4–0.6 *(middle-bottom)* and 0.6–0.8 *(bottom)*. We also show the luminosity function of all galaxies for the same redshift ranges in the rightmost panel. The dashed lines show the best fit Schechter function. For all $\hat{e}$ ranges there seems to be an evolutionary trend with redshift.

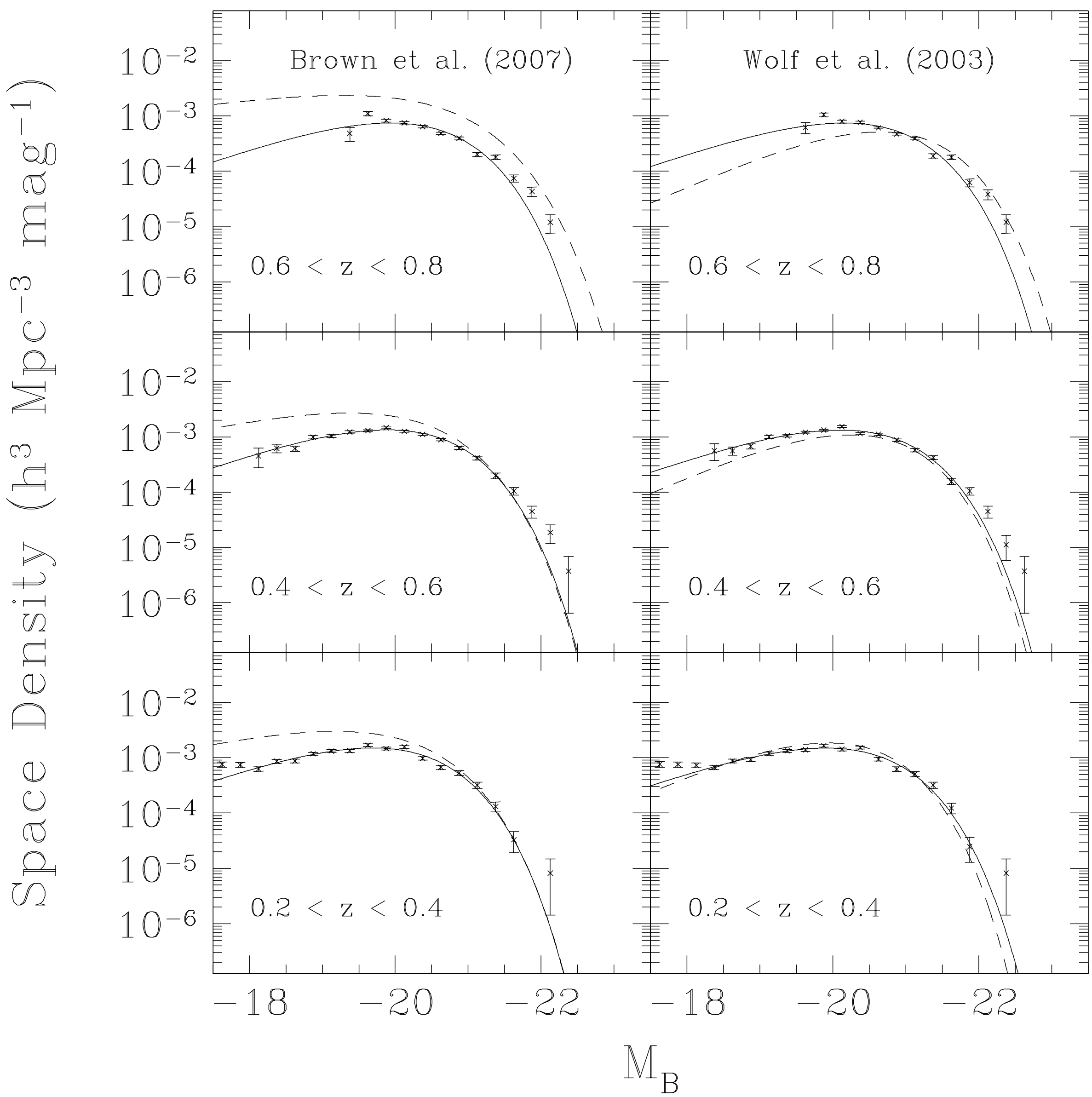

Fig. 15.— Early-type galaxy luminosity functions for the redshift ranges 0.2–0.4 *(bottom)*, 0.4–0.6 *(middle)* and 0.6–0.8 *(top)* from this work *(solid lines and points)* and from Brown et al. (2007, left) and Wolf et al. (2003, right) *(dashed lines)*. Note that the shapes agree well for galaxies brighter than M_*. The difference in the fainter end and in the normalization ϕ_* with the functions of Brown et al. (2007) come from the different selection criteria (see § 5 for details).